

1 **Title page**

2

3 Two distinct phases of chloroplast biogenesis during de-etiolation in *Arabidopsis*  
4 *thaliana*

5

6

7 Authors: Rosa Pipitone<sup>1</sup>, Simona Eicke<sup>2</sup>, Barbara Pfister<sup>2</sup>, Gaetan Glauser<sup>3</sup>, Denis  
8 Falconet<sup>4</sup>, Clarisse Uwizeye<sup>4</sup>, Thibaut Pralon<sup>1</sup>, Samuel Zeeman<sup>2</sup>, Felix Kessler<sup>1,\*</sup>,  
9 Emilie Demarsy<sup>1,5,\*</sup>

10

11 Authors affiliations:

12 <sup>1</sup> Plant Physiology Laboratory, University of Neuchâtel, Neuchâtel, Switzerland

13 <sup>2</sup> Institute of Molecular Plant Biology, Department of Biology ETH Zurich, Zurich,  
14 Switzerland

15 <sup>3</sup> Neuchâtel Platform of Analytical Chemistry, University of Neuchâtel, Neuchâtel,  
16 Switzerland

17 <sup>4</sup> Univ. Grenoble Alpes, CNRS, CEA, INRAE, IRIG-DBSCI-LPCV, 38000 Grenoble,  
18 France

19 <sup>5</sup> Department of Botany and Plant Biology, University of Geneva, CH-1211 Geneva 4,  
20 Switzerland

21

22

23 \*Corresponding authors:

24 Emilie Demarsy, [emilie.demarsy@unige.ch](mailto:emilie.demarsy@unige.ch)

25 Felix Kessler, [felix.kessler@unine.ch](mailto:felix.kessler@unine.ch)

26

27 Running title (max 50 characters):

28 Dynamics of chloroplast biogenesis

29

30 Impact statement: Serial Block Face Scanning Electron Microscopy (SBF-SEM) associated  
31 with biomolecular analysis show that chloroplast differentiation proceeds by distinct 'Structure  
32 Establishment' and 'Chloroplast Proliferation' phases, each with differential protein and lipid  
33 regulation.

34

35

36 **Keywords**

37 Thylakoid / Chloroplast / Photosynthesis / SBF-SEM / Proteomics / Arabidopsis

38

39

41

## 42 **Abstract**

43

44 Light triggers chloroplast differentiation whereby the etioplast transforms into a  
45 photosynthesizing chloroplast and the thylakoid rapidly emerges. However, the sequence of  
46 events during chloroplast differentiation remains poorly understood. Using Serial Block Face  
47 Scanning Electron Microscopy (SBF-SEM), we generated a series of chloroplast 3D  
48 reconstructions during differentiation, revealing chloroplast number and volume and the extent  
49 of envelope and thylakoid membrane surfaces. Furthermore, we used quantitative lipid and  
50 whole proteome data to complement the (ultra)structural data, providing a time-resolved, multi-  
51 dimensional description of chloroplast differentiation. This showed two distinct phases of  
52 chloroplast biogenesis: an initial photosynthesis-enabling 'Structure Establishment Phase'  
53 followed by a 'Chloroplast Proliferation Phase' during cell expansion. Moreover, these data  
54 detail thylakoid membrane expansion during de-etiolation at the seedling level and the relative  
55 contribution and differential regulation of proteins and lipids at each developmental stage.  
56 Altogether, we establish a roadmap for chloroplast differentiation, a critical process for plant  
57 photoautotrophic growth and survival.

58

59

60

## 61 Introduction

62

63 Seedling development relies on successful chloroplast biogenesis, ensuring the transition from  
64 heterotrophic to autotrophic growth. Light is a crucial factor for chloroplast differentiation. For  
65 seeds that germinate in the light, chloroplasts may differentiate directly from proplastids  
66 present in cotyledons. However, as seeds most often germinate underneath soil, seedling  
67 development typically begins in darkness and follows a skotomorphogenic program called  
68 etiolation, characterized by rapid hypocotyl elongation and etioplast development. Light  
69 promotes seedling de-etiolation, which involves a series of morphological changes, such as  
70 cotyledon expansion, hypocotyl growth inhibition, and greening, that accompanies the onset  
71 of photosynthesis in chloroplasts. During de-etiolation, etioplast–chloroplast transition is  
72 thereby rapidly triggered by light following seedling emergence at the soil surface (Solymosi  
73 and Schoefs, 2010; Weier and Brown, 1970). A hallmark of chloroplast differentiation is the  
74 biogenesis of thylakoids, a network of internal membranes where the components of the  
75 photosynthetic electron transport chain assemble. Thylakoid biogenesis and the onset of  
76 photosynthesis rely on the concerted synthesis and coordinated assembly of lipids and  
77 proteins in both space and time.

78

79 The thylakoids harbor the photosynthetic electron transport chain, which is composed of three  
80 complexes: photosystem II (PSII), the cytochrome *b<sub>6</sub>f* complex (Cyt *b<sub>6</sub>f*), and photosystem I  
81 (PSI). Electron transfer between these complexes is facilitated by mobile electron carriers,  
82 specifically the low-molecular-weight, membrane-soluble plastoquinone (electron transfer from  
83 PSII to Cyt *b<sub>6</sub>f*) and the lumenal protein plastocyanin (electron transfer from Cyt *b<sub>6</sub>f* to PSI).  
84 Electron transfer leads to successive reduction and oxidation of electron transport chain  
85 components. The final reduction step catalyzed by ferredoxin-NADP(+) reductase (FNR) leads  
86 to NADPH production. Oxidation of water by PSII and of plastoquinone by Cyt *b<sub>6</sub>f* releases  
87 protons into the lumen, generating a proton gradient across the thylakoid membrane that drives  
88 the activity of the thylakoid-localized chloroplast ATP synthase complex. Each of the  
89 photosynthetic complexes consists of multiple subunits encoded by the plastid or nuclear  
90 genome. PSII and PSI have core complexes comprising 25–30 and 15 proteins, respectively  
91 (Amunts and Nelson, 2009; Caffarri et al., 2014). The antenna proteins from the Light  
92 Harvesting Complexes (LHC) surround the PSI and PSII core complexes contributing to the  
93 formation of supercomplexes. Cyt *b<sub>6</sub>f* is an eight-subunit dimeric complex. Each complex of  
94 the electron transport chain has a specific dimension, orientation, and location within the  
95 thylakoid membrane, occupying a defined surface, and their dimensions have been reported  
96 in several studies giving congruent results (Caffarri et al., 2014; Kurisu et al., 2003; Van

97 Bezouwen et al., 2017). During de-etiolation, massive protein synthesis is required for  
98 assembly of the highly abundant photosynthetic complexes embedded in thylakoids.  
99 Chloroplast proteins encoded by the nuclear genome must be imported from the cytoplasm.  
100 The general chloroplast protein import machinery is composed of the multimeric complexes  
101 Translocon of Outer membrane Complex (TOC) and Translocon of Inner membrane Complex  
102 (TIC), and selective import is based on specific recognition of transit peptide sequences and  
103 TOC receptors (Agne and Kessler, 2010; Richardson and Schnell, 2019).

104  
105 Reminiscent of their cyanobacterial origin, chloroplast membranes are composed mostly of  
106 glycolipids (mono- and di-galactosyldiacylglycerol; MGDG and DGDG) and are poor in  
107 phospholipids compared to other membranes in the cell (Bastien et al., 2016; Block et al.,  
108 1983; Kobayashi, 2016). Galactolipids comprise a glycerol backbone esterified to contain a  
109 single (MGDG) or double (DGDG) galactose units at the *sn1* position and two fatty acid chains  
110 at the *sn2* and *sn3* positions. In addition to the number of galactose units at *sn1*, galactolipids  
111 also differ by the length and degrees of saturation of the fatty acid chains. In some species,  
112 including Arabidopsis, galactolipid synthesis relies on two different pathways, defined as the  
113 eukaryotic and prokaryotic pathway depending on the organellar origin of the diacylglycerol  
114 precursor. The eukaryotic pathway requires the import of diacyl-glycerol (DAG) synthesized in  
115 the endoplasmic reticulum (ER) into the plastids and is referred to as the ER pathway, whereas  
116 the prokaryotic pathway is entirely restricted to the plastid (PL) and is referred to as the PL  
117 pathway (Ohlrogge and Browse, 1995). As signatures, ER pathway–derived galactolipids  
118 harbor an 18-carbon chain whereas PL pathway–derived galactolipids harbor a 16-carbon  
119 chain at the *sn2* position. In addition to constituting the lipid bilayer, galactolipids are integral  
120 components of photosystems and thereby contribute to photochemistry and photoprotection  
121 (Aronsson et al., 2008; Kobayashi, 2016). Thylakoids also contain neutral lipids such as  
122 chlorophyll, carotenoids, tocopherols, and plastoquinone. These may exist freely or be  
123 associated with the photosynthetic complexes, having either a direct role in photosynthesis  
124 (chlorophyll, carotenoids, plastoquinone) or participating indirectly in the optimization of light  
125 usage and/or mitigation of potentially damaging effects (tocopherols in addition to carotenoids  
126 and plastoquinone) (Hashimoto et al., 2003; Van Wijk and Kessler, 2017).

127  
128 Past studies used conventional electron microscopy to first describe the architecture of the  
129 thylakoid membrane network. Based on these 2D observations, researchers proposed that  
130 plant thylakoid membranes are organised as single lamellae connected to appressed multi-  
131 lamellar regions called grana. How these lamellae are interconnected was revealed only later  
132 following the development of 3D electron microscopic techniques. Tremendous technological  
133 progress in the field of electron microscopy has been made recently, leading to improved

134 descriptions of chloroplast ultrastructure (Daum et al., 2010; Daum and Kühlbrandt, 2011).  
135 Electron tomography substantially improved our comprehension of the 3D organisation of the  
136 thylakoid network in chloroplasts at different developmental stages and in different  
137 photosynthetic organisms, including *Arabidopsis* (Austin and Staehelin, 2011; Liang et al.,  
138 2018), *Chlamydomonas* (Engel et al., 2015), runner bean (Kowalewska et al., 2016), and  
139 *Phaeodactylum tricornutum* (Flori et al., 2017). Electron tomography also provided quantitative  
140 information on thylakoid structure such as the thylakoid layer number within the grana stack  
141 and the thickness of the stacking repeat distance of grana membrane (Daum et al., 2010;  
142 Kirchhoff et al., 2011). These quantitative data allowed a greater understanding of the spatial  
143 organisation of the thylakoid membrane in relation to the embedded photosynthetic complexes  
144 (Wietrzynski et al., 2020). Although electron tomography offers extraordinary resolution at the  
145 nanometer level, its main drawback is a limit to the volume of the observation, enabling only a  
146 partial 3D reconstruction of a chloroplast. SBF-SEM technology allows a much larger volume  
147 to be studied and reconstructed in 3D to show cellular organisation (Peddie and Collinson,  
148 2014; Pinali and Kitmitto, 2014).

149  
150 In combination with electron microscopy, biochemical fractionation of thylakoids has revealed  
151 differential lipid and protein compositions of the grana and the stroma lamellae. The grana are  
152 enriched in DGDG and PSII whereas the stroma lamellae are enriched in MGDG, Cyt *b6/f*, and  
153 PSI (Demé et al., 2014; Koochak et al., 2019; Tomizioli et al., 2014; Wietrzynski et al., 2020).  
154 Changes in lipid and protein compositions during etioplast–chloroplast transition are tightly  
155 linked to the thylakoid architecture. In particular, changes in MGDG to DGDG ratio are  
156 correlated with the transition from prolamellar body (PLB) and prothylakoid (PT) structures  
157 (tubular membrane) to thylakoid membranes (lamellar structure) (Bottier et al., 2007; Demé et  
158 al., 2014; Mazur et al., 2019).

159  
160 Individual studies have provided much insight regarding specific dynamics of the soluble  
161 chloroplast proteome, the chloroplast transcriptome, photosynthesis-related protein  
162 accumulation and photosynthetic activity, chloroplast lipids, and changes in thylakoid  
163 architecture (Armarego-Marriott et al., 2019; Dubreuil et al., 2018; Kleffmann et al., 2007;  
164 Kowalewska et al., 2016; Liang et al., 2018; Rudowska et al., 2012). However, these studies  
165 were mostly qualitative, focused on one or two aspects, and were performed in different model  
166 organisms. Therefore, chemical data related to thylakoid biogenesis remain sparse and  
167 quantitative information is rare. Here, we present a systems-level study that integrates  
168 quantitative information on ultrastructural changes of the thylakoids with lipid and protein  
169 composition during de-etiolation of *Arabidopsis* seedlings.

170

171

172

173

174

## 175 Results

### 176 The photosynthetic machinery is functional after 14 h of de-etiolation

177  
178 We analysed etioplast–chloroplast transition in Arabidopsis seedlings grown in the absence of  
179 exogenous sucrose for 3 days in darkness and then exposed to constant white light (Figure  
180 1A). These experimental conditions were chosen to avoid effects of exogenous sucrose on  
181 seedling development and variations due to circadian rhythm. Upon illumination, the etiolated  
182 seedlings switched from the skotomorphogenic to the photomorphogenic developmental  
183 program, evidenced by opening of the apical hook and cotyledon greening and expansion  
184 (Figure 1B). We stopped the analysis following 96 h of illumination (T96), before the  
185 emergence of the primary leaves. Samples were collected at different selected time points  
186 during de-etiolation(Figure 1A).

187 In angiosperms, chlorophyll synthesis arrests in the dark but starts immediately upon seedling  
188 irradiation (Von Wettstein et al., 1995). Chlorophyll levels in whole seedlings increased within  
189 the first 4 h of illumination (T4) and continued to increase linearly during subsequent  
190 illumination as the seedlings grew (Figure 1C). To evaluate photosynthetic efficiency during  
191 de-etiolation, we measured chlorophyll fluorescence and calculated the maximum quantum  
192 yield of PSII (Fv/Fm, Figure 1D and Figure 1- figure supplement 1). PSII maximum quantum  
193 yield increased during the initial period of illumination and was near the maximal value of 0.8  
194 at 14 h of light exposure (T14), independent of light intensity (Figure 1D and Figure 1- figure  
195 supplement 1A). Other photosynthetic parameters (photochemical quenching, qP and PSII  
196 quantum yield in the light,  $\Phi$ PSII, Figure 1-figure supplement 1 B and C) reached maximum  
197 values at T14 and remained stable thereafter, indicating that the assembly of fully functional  
198 photosynthetic machinery occurs within the first 14 h of de-etiolation, and that further  
199 biosynthesis of photosynthesis related compounds is efficiently coordinated.

200

### 201 Major thylakoid structural changes occur within 24 h of de-etiolation

202  
203 We determined the dynamics of thylakoid biogenesis during the etioplast–chloroplast transition  
204 by observing chloroplast ultrastructure in cotyledons using transmission electron microscopy  
205 (TEM) (Figure 2). Plastids present in cotyledons of etiolated seedlings displayed the typical  
206 etioplast ultrastructure with a paracrystalline PLB and tubular PTs (Figure 2A). The observed  
207 PLBs were constituted of hexagonal units with diameters of 0.8–1  $\mu$ m (Figure 2E). By T4, the  
208 highly structured PLBs progressively disappeared and thylakoid lamellae were formed (Figure  
209 2B). The lamellae were blurry and their thickness varied between 15 and 70 nm (Figure 2F).  
210 After 24 h of illumination (T24), the density of lamellae per chloroplast was higher than that at

211 T4 due to an increase in lamellar length and number. Appressed regions corresponding to  
212 developing grana stacks also appeared by T24 (Figure 2C and G). These early grana stacks  
213 consisted of 2–6 lamellae with a thickness of 13 nm each (Figure 2- figure supplement 1). In  
214 addition, starch granules were present at T24, supporting the notion that these chloroplasts  
215 are photosynthetically functional and able to assimilate carbon dioxide (CO<sub>2</sub>). At T96, thylakoid  
216 membrane organisation was visually similar to that at T24, but with more layers per grana (up  
217 to 10 lamellae per grana; Figures 3D and H). In addition, singular lamella thickness at T96  
218 increased by 2–3 nm compared to that at T24 (Figure 2- figure supplement 1). The major  
219 differences observed between T24 and T96 were increases in starch granule size and number  
220 and overall chloroplast size. Etioplast average length (estimated by measuring the maximum  
221 distance on individual slices) was 2 µm (± 0.9, n=10) in the dark (T0), whereas chloroplast  
222 average length was 6 µm (± 1.62, n=10) at T96 (Table1). Collectively, these data show that  
223 photosynthetically functional thylakoid membranes form rapidly during the first 24 h of de-  
224 etiolation. This implies that there are efficient mechanisms for thylakoid assembly and  
225 structural organisation. Subsequent changes seem to involve the expansion of pre-existing  
226 structures (i.e. lamellae length and grana size) and the initiation of photosynthetic carbon  
227 fixation (reflected by starch content).

228

229

230

### 231 Quantitative analysis of thylakoid surface area per chloroplast during de-etiolation

232

233 To visualize entire chloroplasts and thylakoid networks in 3D, and to obtain a quantitative view  
234 of the total thylakoid surface area during chloroplast development, we prepared and imaged  
235 cotyledons at different developmental stages by SBF-SEM (Figure 3 A-D). PLBs, thylakoids,  
236 and envelope membranes were selected, and segmented images were used for 3D  
237 reconstruction (Figure 3E–N, and videos 1–4; see also Figure 2- figure supplement 1 and  
238 Figure 4- figure supplement 1 for grana segmentation). Similar to that observed by TEM  
239 (Figure 2), a drastic switch from PLB to thylakoid membrane occurred by T4: the typical  
240 structure of the PLB connected to PTs disappeared leaving only elongated lamellar structures  
241 (Figure 3E–F and videos 1 and 2). At T24 and T96, thylakoid membranes were organised in  
242 appressed and non-appressed regions and large spaces occupied by starch granules were  
243 observed (Figure 3G–H and videos 3 and 4). 3D reconstruction revealed a change in plastid  
244 shape from ovoid at T0 and T4 to hemispheric at T24 and T96 (Figure 3I–N).

245



246 Using 3D reconstruction of the thylakoid network for 3 or 4 chloroplasts for each developmental  
247 stage, quantitative data such as chloroplast volume and membrane surface area were  
248 extracted and calculated (Figure 4A and B, Figure 4 figure supplement 1 and Table 1). The  
249 total chloroplast volume increased about 11-fold from T4 ( $9.4 \mu\text{m}^3$ ) to T96 ( $112.14 \mu\text{m}^3$ ) (Table  
250 1). In parallel, the thylakoid surface area increased about 30-fold reaching  $2,086 (\pm 393) \mu\text{m}^2$   
251 per chloroplast at T96 (Figure 4A and Table 1). The surface area increased drastically between  
252 T4 and T24 (about 22-fold) and much less (about 1.4-fold) between T24 and T96. Accordingly,  
253 quantification of the envelope surface area indicated that the ratio of the thylakoid to envelope  
254 surface area increased drastically from T4 to T24, but decreased slightly between T24 and  
255 T96 (Table 1).

256 Our observations indicated that chloroplast development during the first 96 hours of de-  
257 etiolation could be separated into two phases: a first phase reflected by qualitative changes  
258 (i.e. structure establishment and reorganisation of the thylakoid network architecture) and a  
259 second phase (starting before T24) during which thylakoid surface increased due to the  
260 expansion and stacking of lamellae. We further analysed these temporal processes at the  
261 molecular level focusing on proteins and lipids that constitute the thylakoid membrane.

262  
263

## 264 Dynamics of plastid proteins related to thylakoid biogenesis

265

266 We analysed the full proteome to reveal the dynamics of protein accumulation during de-  
267 etiolation. Total proteins were prepared from 3-day-old etiolated seedlings exposed to light for  
268 0–96 h (eight time points; Figure 1A) and quantified by label-free shot-gun mass spectrometry.  
269 For relative quantification of protein abundances between different samples, peptide ion  
270 abundances were normalized to total protein (see Materials and Methods). We considered  
271 further only those proteins that were identified with a minimum of two different peptides (with  
272 at least one being unique; see Methods for information on protein grouping), resulting in the  
273 robust identification and quantification of more than 5,000 proteins. Fold changes of protein  
274 abundances between two time points were regarded as significant if their adjusted  $p$ -value (i.e.  
275 the  $q$ -value) was  $< 0.01$ .

276 The first 12 h of illumination (T12) saw very few significant changes in protein abundance  
277 (Supplemental Dataset 1). After 8 h of illumination (T8), we observed decreased abundance  
278 of only one protein (the photoreceptor cryptochrome 2, consistent with its photolabile property)  
279 and increased levels of only three proteins, which belonged to the chlorophyll  $a/b$  binding  
280 proteins category involved in photoprotection (AT1G44575 = PsbS; AT4G10340= Lhcb5;  
281 AT1G15820= Lhcb6; (Chen et al., 2018; Li et al., 2000). A drastic change of proteome  
282 composition occurred by T24, with 467 proteins showing a significant increase in abundance

283 with over 2-fold change ( $FC > 2$ ) compared with the etiolated stage, and 150 proteins showing  
284 a significant decrease with over 2-fold change ( $FC < 0.5$ ). As expected, the 100 most-  
285 upregulated proteins comprised proteins related to photosynthesis, proteins constituting the  
286 core and antennae of photosystems, and proteins involved in carbon fixation (Supplemental  
287 Dataset 1).

288 To monitor the dynamics of the plastidial proteome, we selected proteins predicted to localize  
289 to the plastid (consensus localization from SUBA4; Hooper et al., 2017). Generation of a global  
290 heatmap for each of the 1,112 potential plastidial proteins revealed different accumulation  
291 patterns (Supplemental Dataset 2 and Figure 5- figure supplement 1). Hierarchical clustering  
292 showed a categorization into six main clusters. Cluster 1 (purple) contained proteins whose  
293 relative amounts decreased during de-etiolation. Clusters 2, 5, and 6 (pink, light green, and  
294 dark green, respectively) contained proteins whose relative amounts increased during de-  
295 etiolation but differed with respect to the amplitude of variations. Proteins in clusters 2 and 6  
296 displayed the largest amplitude of differential accumulation. Gene ontology (GO) analysis (Mi  
297 et al., 2019) indicated a statistically significant overrepresentation of proteins related to the  
298 light reactions of photosynthesis in clusters 2 and 6 (Supplemental Dataset 2).  
299 Underrepresentation of organic acid metabolism, in particular carboxylic acid metabolism,  
300 characterized cluster 2, whereas overrepresentation of carboxylic acid biosynthesis and  
301 underrepresentation of photosynthetic light reactions were clear features of cluster 3. Protein  
302 levels in cluster 3 changed only moderately during de-etiolation in contrast with proteins levels  
303 in cluster 2. No biological processes were significantly over- or underrepresented in clusters  
304 1, 4, and 5.

305 To analyse the dynamics of proteins related to thylakoid biogenesis, we selected specific  
306 proteins and represented their pattern of accumulation during de-etiolation (Figure 5). We  
307 included proteins constituting protein complexes located in thylakoids (complexes constituting  
308 the electron transport chain and the ATP synthase complex) and proteins involved in  
309 chloroplast lipid metabolism, chlorophyll synthesis, and protein import into the chloroplast. In  
310 agreement with that depicted in the global heatmap (Figure 5- figure supplement 1), all  
311 photosynthesis-related proteins increased in abundance during de-etiolation (Figure 5A).  
312 However, our hierarchical clustering did not show any particular clustering per complex. Only  
313 few chloroplast-localized proteins related to lipid biosynthesis were present in our proteomics  
314 data set. Among the eight detected proteins, two appeared differentially regulated; fatty acid  
315 binding protein 1 (FAB1) and fatty acid desaturase 7 (FAD7) levels increased only between 72  
316 h of illumination (T72) and T96, whereas the other proteins gradually accumulated over the  
317 course of de-etiolation (Figure 5B). Etioplasts initiate synthesis of chlorophyll precursors that  
318 are blocked at the level of protochlorophyllide synthesis, with protochlorophyllide  
319 oxidoreductase A (PORA) in its inactive form accumulating to high levels in the etioplast before

320 subsequently decreasing at the protein level upon activation and degradation following light  
321 exposure (Blomqvist et al., 2008; Runge et al., 1996; Von Wettstein et al., 1995). In agreement,  
322 illumination resulted in increased amounts of all detected proteins of the chlorophyll  
323 biosynthesis pathway, except PORA, which clearly decreased and was separated from other  
324 chlorophyll-related proteins (Figure 5C). We also selected proteins involved in protein import  
325 in chloroplasts, focusing on the TOC-TIC machinery (Figure 5D) that is the major route for  
326 plastid protein import and essential for chloroplast biogenesis (Kessler and Schnell, 2006).  
327 Past studies identified several TOC preprotein receptors that are proposed to display  
328 differential specificities for preprotein classes (Bauer et al., 2000; Bischof et al., 2011). The  
329 composition of plastid import complexes varies with developmental stages and in different  
330 tissues, thereby adjusting the selectivity of the import apparatus to the demands of the plastid  
331 and influencing its proteome composition (Demarsy et al., 2014; Kubis et al., 2003).  
332 Accordingly, the TOC receptors TOC120 and TOC132, which are important for the import of  
333 proteins in non-photosynthetic tissues, were more abundant in etioplasts compared to fully-  
334 developed chloroplasts (compare T0 and T96). TOC120 and TOC132 were part of a cluster  
335 separated from other components of the plastid machinery, such as the TOC159 receptor  
336 associated with large-scale import of proteins in chloroplasts. The general import channel  
337 TOC75 (TOC75 III) maintained stable expression levels throughout de-etiolation, reflecting its  
338 general role in protein import. All other components clustered with TOC159 and displayed  
339 gradual increases in accumulation during de-etiolation. Most of these components have not  
340 been reported to confer selectivity to the import machinery, which suggests an overall increase  
341 of chloroplast protein import capacity.

342

343

344 To validate and complement our proteomic data, we used immunoblot analysis to detect and  
345 quantify representative proteins of the photosynthetic complexes. Overall, immunoblot and  
346 proteomics provided similar results (Figure 6 and Figure 6- figure supplement 1). PsbA and  
347 PsbD (PSII reaction center core), PsbO (Oxygen Evolving Complex), and Lhcb2 (outer  
348 antenna complex) proteins were detectable in seedlings at T0, gradually increasing thereafter.  
349 Accumulation of the PSI proteins PsaC and PsaD and the Cyt *b<sub>6</sub>f* complex protein PetC started  
350 later; these proteins were detectable starting at T8 (Figure 6A and Figure 6- figure supplement  
351 1). Interestingly, AtpC (ATP synthase complex) was detectable in the etioplast, as described  
352 previously (Plöscher et al., 2011). Other proteins were selected as markers of etioplast-  
353 chloroplast transition. As expected, ELIPs (Early Light Induced Protein) transiently  
354 accumulated upon the dark-to-light transition (Figure 6A) (Kimura et al., 2003). As in the  
355 proteome analysis, PORA accumulated in etiolated seedlings (T0) and then progressively  
356 disappeared upon light exposure. We performed absolute quantification for PsbA, PsaC, and

357 PetC proteins using recombinant proteins as standards (Figure 6B and C and Figure 6- figure  
358 supplement 1). Quantitative data (nmol/seedling) were obtained and normalized using the last  
359 time point (Figure 6C) to compare the dynamics of protein accumulation. In addition, the  
360 comparison of PsbA and PsaC (representative proteins of PSII and PSI, respectively) showed  
361 that PsbA levels were about twice that of PsaC at T96 (Figure 6B and C).

362

363

#### 364 Dynamics of chloroplast membrane lipids

365

366 Total lipids were extracted from seedlings collected at different time points during de-etiolation  
367 (T0, T4, T8, T12, T24, T48, T72, and T96), analysed by ultra-high pressure liquid  
368 chromatography–mass spectrometry (UHPLC-MS), and quantified against pure standards  
369 (supplemental Dataset 3). We analysed the quantity and kinetics of accumulation of 12  
370 different species of galactolipids (Figure 7A and B). MGDG 18:3/16:3, MGDG 18:3/18:3,  
371 MGDG 18:3/16:1, DGDG 18:3/18:3, and DGDG 18:3/16:0 were the most abundant lipids  
372 detected at all time points. Accumulation of all galactolipids increased upon de-etiolation;  
373 however, clustering analysis identified two distinct kinetic patterns. One group displayed a leap  
374 between T8 and T12, whereas the other group showed a more gradual increase during the de-  
375 etiolation period (Figure 7C). Interestingly, the two clusters separated the lipids according to  
376 the two pathways described for galactolipid synthesis, namely the ER and PL pathways (Figure  
377 7A and B) (Marechal et al., 1997; Ohlrogge and Browse, 1995). During early stages of de-  
378 etiolation (T0–T24), we observed an incremental accumulation of MGDG and DGDG  
379 galactolipids derived from the ER pathway, whereas galactolipids from the PL pathway started  
380 to accumulate at T24 (Figure 7A and B). The MGDG/DGDG ratio decreased between T0 and  
381 T8. This was associated with the transition from PLB (cubic lipid phase) to thylakoid membrane  
382 (lamellar structure) (Bottier et al., 2007). The MGDG/DGDG ratio started to increase gradually  
383 at T8 and was constant by T72 and T96 (Figure 7D).

384

385

386

#### 387 Identification of a chloroplast division phase

388

389 We observed a massive increase in the accumulation of photosynthesis-related proteins and  
390 galactolipids between T24 and T96, corresponding to  $FC > 2$  in the levels of all major chloroplast  
391 proteins and lipids (Figures 6 and 7). Intriguingly, the total thylakoid surface per chloroplast  
392 increased by only 41 % between these two time points (Figure 4A and Table 1). We reasoned  
393 that the increase in chloroplast proteins and lipids between T24 and T96 could be explained

394 by increased chloroplast number (per cell and thus per seedling) and thus total thylakoid  
395 surface per seedling. We therefore determined chloroplast number per cell and the cell number  
396 and volume for each developmental stage through SBF-SEM analysis (T0, T4, T24, and T96)  
397 and confocal microscopy analysis for intermediary time points (T24–T96) (Figure 8 and Figure  
398 8- figure supplement 1). The chloroplast number per cell was constant from T4 ( $25 \pm 8$ ) to T24  
399 ( $26 \pm 6$ ); however, in parallel with cell expansion (Figure 8A and B), chloroplast number  
400 increased sharply (4-fold increase) between T24 ( $26 \pm 6$ ) and T96 ( $112 \pm 29$ ), indicating that  
401 two rounds of chloroplast division occurred during this time. Immunoblot analysis of  
402 FILAMENTOUS TEMPERATURE-SENSITIVE FtsZ1, FtsZ2-1, and FtsZ2-2 proteins showed  
403 that these key components of the chloroplast division machinery were already present during  
404 the early time points of de-etiolation. We observed considerably increased accumulation of  
405 these proteins between T24 and T48, consistent with the idea that activation of chloroplast  
406 division takes place at T24, leading the proliferation of chloroplasts (Figure 8C–D). However,  
407 levels of ACCUMULATION AND REPLICATION OF CHLOROPLAST 5 (ARC5) protein,  
408 another key component of the chloroplast division machinery, clearly increased during de-  
409 etiolation between T8 and T12, presumably reflecting assembly of the chloroplast division  
410 machinery before its activation and the proliferation of chloroplasts (Figure 8D). To test  
411 whether there is a correlation between chloroplast division and either volume or developmental  
412 stage, we measured the volume of dividing chloroplasts at T24 and T96 using images acquired  
413 by SBF-SEM (Figure 8E and Figure 4B). The average size of dividing chloroplasts at T24 was  
414 higher than the average size of all chloroplasts ( $96 \mu\text{m}^3$  compared to  $62 \mu\text{m}^3$ ). The volume of  
415 dividing chloroplasts at T96 was consistently higher than  $100 \mu\text{m}^3$  although some of the  
416 chloroplasts present were smaller (Figure 8E and Figure 4B). Altogether, this indicates that  
417 developing chloroplasts only divide once a certain chloroplast volume is reached.

418

### 419 Model of thylakoid surface expansion over time

420

421 During de-etiolation, thylakoid surface increased with the accumulation of galactolipids and  
422 photosynthesis-related proteins, leading to the formation of functional chloroplasts. To  
423 determine the thylakoid membrane surface area per seedling and its expansion over time, we  
424 first calculated the surface area occupied by the main galactolipids (MGDG and DGDG) and  
425 photosynthetic complexes (PSII, Cyt *b<sub>6</sub>f* and PSI) per seedling (Table 2).

426 Equation 1:

$$427 \text{Surface/seedling} = \text{nmol/seedling} * N * \text{nm}^2 \text{ per molecule}$$

428

429 Quantitative data for MGDG, DGDG, PsbA, PetC, and PsaC (nmol/seedling) obtained from  
430 lipidomic and immunological analyses (Figures 6 and 7) were converted into number of  
431 molecules/seedling using the Avogadro constant ( $N$ ). To calculate the surface area exposed  
432 to the stroma and account for the lipid double layer of the membrane, corresponding values of  
433 lipids (Figure 4A) were divided by 2. In addition, the lipid values were corrected by subtracting  
434 the portion of lipids incorporated into the envelope rather than present in the thylakoids (Table  
435 1, Table 2 and Supplemental Dataset 3). The surface area occupied by molecules of MGDG  
436 and DGDG, and that of PSII, Cyt  $b_6f$ , and PSI photosynthetic complexes (nm<sup>2</sup> per molecule,  
437 corresponding to stroma-exposed surface) were retrieved from the literature (Table 3).  
438 Specifically, we used the minimal molecular area of MGDG and DGDG (Bottier et al., 2007).  
439 To quantify the surface area occupied by the galactolipids and photosynthetic complexes in  
440 thylakoids per seedling, the number of molecules per seedling of galactolipids was multiplied  
441 by the corresponding molecular surface area, whereas the number of molecules per seedling  
442 of PsbA, PetC, and PsaC (subunits of PSII, Cyt  $b_6f$ , and PSI, respectively) were multiplied by  
443 the surface area of the corresponding complex (see Table 3).  
444 We calculated thylakoid surface ( $S$ ) per seedling for each time point ( $t$ ) as the sum of the surface  
445 occupied by MGDG, DGDG, photosynthetic complexes (PS), and  $\epsilon$  per seedling, the latter of  
446 which corresponds to compounds such as other lipids (e.g. sulfoquinovosyldiacylglycerol,  
447 plastoquinone) or protein complexes (ATP synthase and NDH) that were not quantified.

448 Equation 2:

$$449 \quad S_{thylakoid}(t)/seedling = (S_{MGDG}(t) + S_{DGDG}(t) + S_{PS}(t) + \epsilon)/seedling$$

450

451 Omitting the unknown  $\epsilon$  factor, we plotted the thylakoid surface calculated for each time point  
452 where quantitative molecular data were available (T0, T4, T8, T12, T24, T48, T72, and T96)  
453 as a function of the duration of light exposure (Figure 9- figure supplement 1). The best fitting  
454 curve corresponded to a S-shaped logistic function, characterized by a lag phase at early time  
455 points (T0–T8), followed by a phase of near-linear increase, and a final plateau at the final time  
456 points (T72–T96). To model this function, a four-parameter logistic non-linear regression  
457 equation was used to describe the dynamics of the total thylakoid surface over time (Figure 9-  
458 figure supplement 1C).

459

460

## 461 Superimposition of molecular and morphometric data

462

463 We compared the values of thylakoid surface, as obtained with the model based on molecular  
464 data, with the values obtained from the morphometric analysis (Figure 9). The total thylakoid

465 surface per seedling ( $S_{thylakoid\_morpho}$ ) was calculated by multiplying the thylakoid surface  
466 ( $S_{thylakoid}$ ) per chloroplast obtained by morphometrics (Figure 4A) by the number of  
467 chloroplasts ( $nb.cp$ ) per cell (Figure 8A) and the number of cells ( $nb.cells$ ) per seedlings for  
468 each time point ( $t$ ).

469 Equation 3:

$$470 \quad \frac{S_{thylakoid_{morpho}(t)}}{seedling} =$$
$$471 \quad S_{thylakoid}(t)/chloroplast * nb.cp(t)/cell * nb.cells(t)/seedling$$

472

473 We estimated cell number per seedling by measuring the total volume occupied by palisade  
474 and spongy cells in cotyledons (that corresponded to 50% of total cotyledon volume) (Figure  
475 9- figure supplement 2) and dividing this by the average cell volume quantified by Amira  
476 software (Figure 7B). As reported previously (Pyke and Leech, 1994), cell number was  
477 constant during cotyledon development. We estimated this number as 3,000 mesophyll and  
478 palisade cells per seedling at T24 and T96 (Figure 9- figure supplement 2). The thylakoid  
479 membrane surface quantified by the morphometric approach was also estimated at T4,  
480 assuming that cell number per cotyledon remained similar between T4 and T24. We compared  
481 the thylakoid surface predicted by our mathematical model to the surface estimated  
482 experimentally with our 3D thylakoid reconstruction and morphometric measurements (Figure  
483 9 and Table 1). As shown in Figure 9, the two approaches showed very similar total thylakoid  
484 surface area per seedling at T4 and T24 and differences in this parameter by T96.

485

486

487

488

489

490

491

## 491 Discussion

492

493 Here, the analysis of 3D structures of entire chloroplasts in Arabidopsis in combination with  
494 proteomic and lipidomic analyses provide an overview of thylakoid biogenesis. Figure 10  
495 depicts a summary of the changes that occur during the de-etiolation process. When  
496 considering chloroplast development, our study shows that de-etiolation is divided into two  
497 phases. We documented structural changes (disassembly of the PLB and the gradual  
498 formation of thylakoid lamellae) and initial increases of ER- and PL-pathway galactolipids and  
499 photosynthesis-related proteins (PSII, PSI, and Cyt *b<sub>6</sub>f*) during the 'Structure Establishment  
500 Phase', which was followed by increased chloroplast number in parallel with cell expansion in  
501 the 'Chloroplast Proliferation Phase'. Collection of quantitative data allowed us to create a  
502 mathematical model of thylakoid membrane expansion and describe this process during de-  
503 etiolation.

504

### 505 A set of 3D reconstructions of whole chloroplasts by SBF-SEM

506

507 In contrast to electron tomography, which is limited in the volume of observation, SBF-SEM  
508 allows the acquisition of ultrastructural data from large volumes of mesophyll tissue and the  
509 generation of 3D reconstructions of entire cells and chloroplasts (Figure 3 and Figure 8- figure  
510 supplement 1). SEM image resolution was sufficient to visualize stromal lamellae and grana  
511 contours, whereas grana segmentation in different lamellae was deduced according to our  
512 own TEM analysis and literature data (Figure 2- figure supplement 1 and Figure 3- figure  
513 supplement 1). This approach allowed us to obtain quantitative data of chloroplast and  
514 thylakoid structure at different developmental stages during de-etiolation at the whole-  
515 chloroplast level. By T96, the latest time point of our analysis, the total surface area of  
516 thylakoids present in the seedling cotyledons was about 700 mm<sup>2</sup> (see values in Table 1 for  
517 calculation), about 500-fold greater than the surface area of one cotyledon at this  
518 developmental stage. This result is supported by previous estimates made regarding thylakoid  
519 surface area relative to leaf surface area (Bastien et al., 2016; Demé et al., 2014). Moreover,  
520 the extent of thylakoid surface area emphasizes how fast and efficient thylakoid biogenesis is  
521 during plant development, allowing plants to optimize light absorption capacity, ensuring their  
522 primary source of energy.

523

### 524 Chloroplast development: 'Structure Establishment Phase'

525



527 We observed TEM images and quantified 3D chloroplast ultrastructure by SBF-SEM analysis  
528 during chloroplast differentiation. Typical etioplast structure of the PLB connected with tubular  
529 PTs was replaced by lamellar thylakoids by T4. Measurements of PLB diameter and thylakoid  
530 length and thickness were comparable with literature values (Biswal et al., 2013; Daum et al.,  
531 2010; Kirchhoff et al., 2011), indicating that these morphometric values are conserved between  
532 various model organisms. Thylakoid surface increased 20-fold between T4 and T24.  
533 Remarkably, PSII maximum quantum yield (Fv/Fm) reached the maximal value (0.8) by T14,  
534 independent of light intensity (Figure 1D and Figure 1- figure supplement 1). This shows that  
535 PSII assembly, and more globally assembly of the photosynthetic machinery, occurs  
536 simultaneously with thylakoid membrane formation and that photosynthesis is operational  
537 almost immediately upon greening.

538 Our proteomic and lipidomic analyses suggest that chloroplast ultrastructural changes rely on  
539 specifically timed molecular changes. Proteomic analysis revealed the accumulation patterns  
540 of more than 5,000 unique proteins at eight time points during de-etiolation. These data provide  
541 information for plastid development and more widely on light-regulated developmental  
542 processes (Supplemental Dataset 1). Our dataset is more exhaustive regarding temporal  
543 resolution and the number of unique proteins detected than that of previous reports on  
544 chloroplast differentiation and de-etiolation (Bräutigam and Weber, 2009; Plösch et al., 2011;  
545 Reiland et al., 2011; Wang et al., 2006).

546 Here, we focused on chloroplast-localized proteins, specifically on thylakoid membrane  
547 proteins. According to the SUBA4 localization consensus, 1,112 proteins were assigned to  
548 plastids, which covers about a third of the total plastid proteome (Ferro et al., 2003; Hooper et  
549 al., 2017; Kleffmann et al., 2007). Our data suggest that the reorganisation of pre-existing  
550 molecules rather than *de novo* synthesis is responsible for the major chloroplast ultrastructural  
551 changes that occur between T0 and T4. These results are consistent with other studies  
552 reporting only minor increases in protein accumulation and translation during initial chloroplast  
553 differentiation (Dubreuil et al., 2018; Kleffmann et al., 2007; Reiland et al., 2011). GO analysis  
554 combined with expression pattern-based hierarchical clustering highlighted that most  
555 photosynthesis-related proteins are globally coregulated (Figure 5- figure supplement 1,  
556 clusters 2 and 6). However, targeted immunoblot analysis revealed different accumulation  
557 dynamics for specific photosystem subunits: PSI subunits were detected at later time points  
558 than PSII subunits, but thereafter PSI subunit accumulation was faster (Figure 6). The kinetics  
559 of different photosynthetic parameters were consistent with the sequential activation of PSII  
560 and PSI, in particular photochemical quenching, which showed increased oxidation of the  
561 plastoquinone pool by T14 (Figure 1- figure supplement 1). Early accumulation of proteins  
562 such as Lhcb5, -6, and PSBS could be a way to quickly induce photoprotective mechanisms  
563 such as non-photochemical quenching to prevent PSII photodamage during initial

564 photosynthetic machinery assembly. Differences in PSI and PSII accumulation dynamics and  
565 activity have been consistently observed in other chloroplast development experimental  
566 systems, including in *Arabidopsis* cell cultures, during germination and development of  
567 *Arabidopsis* seedlings in the light, and in tobacco leaves upon reillumination after dark  
568 adaptation (Armarego-Marriott et al., 2019; Dubreuil et al., 2018; Liang et al., 2018). The  
569 molecular mechanisms underlying this differential accumulation are currently unknown;  
570 however, preferential localization of the PSI and PSII protein complexes in specific thylakoid  
571 membrane domains (lamellae and grana, respectively) and the time taken to establish these  
572 domains during chloroplast development (i.e. grana appear later than stromal lamellae) may  
573 play influential roles.

574 Chloroplast membranes have a specific composition that differs from that of other cell  
575 membranes. Galactolipids constitute the bulk of the thylakoid membranes, but are mostly  
576 absent from other membrane systems under growth conditions where phosphorus nutrient is  
577 available (Jouhet et al., 2007). MGDG and DGDG represent around 80% of the thylakoid  
578 membrane lipids. The absolute quantification of 12 types of MGDG and DGDG galactolipids  
579 (representing the major forms) revealed specific patterns of accumulation (Figure 7). Results  
580 showed a gradual accumulation of MGDG and DGDG galactolipids derived from the ER  
581 pathway from T8 to T24, whereas galactolipids from the PL pathway started to accumulate  
582 after one day of light exposure (T24). This illustrates the different galactolipid compositions of  
583 etioplasts and chloroplasts: ER-pathway galactolipids are predominant in the etioplast  
584 whereas PL-pathway galactolipids are predominant in the chloroplast. As no significant  
585 changes in lipid accumulation were observed by T4, it appears likely that the emergence of  
586 PTs relies on the existing lipids in the etioplast PLB, as suggested also by Armarego-Marriott  
587 et al. (2019). At later time points, galactolipids from both the ER and PL pathways constitute  
588 the lipid matrix of the thylakoid membrane. How the two galactolipid biosynthesis pathways  
589 are regulated during development and/or upon light treatment remains to be elucidated;  
590 however, we hypothesize that the PL pathway gains traction after T24 when photosynthetic  
591 capacity is fully established.

592

### 593 Chloroplast development: 'Chloroplast Proliferation Phase'

594

595 Chloroplast development continued between T24 and T96, during which thylakoid membranes  
596 acquired grana stacks with more clearly defined organisation (Figure 2). Thylakoid surface  
597 increased by only 41%; however, chloroplasts continued to enlarge at a rate comparable to  
598 previous de-etiolation stages (T0–T24). This chloroplast volume expansion may be caused by  
599 enlargement of extra-thylakoidal spaces occupied by emerging starch granules. These results

600 suggest that large amounts of lipids and proteins are necessary to build up the thylakoid  
601 membrane until T24, whereas increases in lipids and proteins between T24 and T96 enable  
602 the expansion of already functional thylakoid membranes in preparation for chloroplast  
603 division. Indeed, chloroplast number per cell increased during de-etiolation, a process that  
604 depends on the division of pre-existing chloroplasts.

605 Both chloroplasts and mitochondria divide through the activity of supramolecular complexes  
606 that constitute the organelle division machineries (Yoshida, 2018). As chloroplast proliferation  
607 was observed between T24 and T96, chloroplast division may correlate with developmental  
608 stage of the organelle. Components of the chloroplast division machinery (e.g. FtsZ and ARC5)  
609 were detectable in etioplasts; however, their protein levels accumulated significantly during de-  
610 etiolation as chloroplasts proliferated (Figure 8C and D). Interestingly, the capacity to divide  
611 appeared to correlate with a minimum chloroplast volume of about  $100 \mu\text{m}^3$ , even at T24 when  
612 most chloroplasts were smaller (Figure 8E and Figure 4B). Whether and how chloroplast size  
613 and developmental stage can be sensed to activate the chloroplast division machinery remains  
614 poorly understood and requires further study.

615

## 616 A model of thylakoid expansion

617

618 Our mathematical model describing the expansion of thylakoid surface per seedling over time  
619 considered the surface area occupied by the membrane lipids MGDG and DGDG and the  
620 major photosynthetic complexes PSII, PSI, and Cyt *b<sub>6</sub>f*. We omitted some components that  
621 contribute to the total thylakoid membrane surface (e.g. the protein complexes ATP synthase  
622 and NDH, and the lipid sulfoquinovosyldiacylglycerol; together grouped as 'ε' in Equation 2).  
623 The predictions made by our model fit the surface estimated by SBF-SEM at T4 and T24,  
624 whereas they do not fit that at T96. This means that compounds used to generate the  
625 mathematical model appear to contribute most to changes in thylakoid surface during early  
626 stages of de-etiolation (the structure establishment phase). By contrast, during the later stages  
627 of de-etiolation (the chloroplast proliferation phase), the contribution of other compounds  
628 omitted in our model is obviously required to build up thylakoid surface.

629 Our proteomics data (Figure 5- figure supplement 1 and Dataset 2) revealed some proteins  
630 that increased between T24 and T96, such as the FtsH protease (AT2G30950). FtsH  
631 proteases have a critical function during thylakoid biogenesis. In Arabidopsis, they constitute  
632 a hetero-hexameric complex of four FtsH subunits, which is integrated in the thylakoid  
633 membrane (Kato and Sakamoto, 2018). Although the FtsH complex surface area is unknown  
634 in Arabidopsis, it can be considered as a potential compound contributing to the thylakoid  
635 surface changes missing from our mathematical model. Other proteins, such as those involved

636 in carotenoid biosynthesis (AT3G10230) or fatty acid metabolism (AT1G08640), also  
637 increased significantly after T24, implying that they contribute to the 'ε' factor.

638 A follow-up study would be to test the model under different conditions to investigate how this  
639 biological system responds to internal (perturbing hormone concentrations, genetic  
640 modification of thylakoid lipid and protein composition) or external (different qualities of light)  
641 factors. This could be instrumental in revealing new potential regulatory mechanisms of  
642 thylakoid biogenesis and maintenance.

643 Upon de-etiolation, the development of photosynthetic capacity relies on successful  
644 chloroplast biogenesis. At the cellular level, this process is expected to be highly coordinated  
645 with the metabolism and development of other organelles. Lipid synthesis involves lipid  
646 exchanges between chloroplasts and the endoplasmic reticulum. How lipid trafficking is  
647 organised remains poorly understood, but could require membrane contact sites between  
648 these two organelles (Michaud and Jouhet, 2019). Physical interaction between mitochondria  
649 and chloroplasts have been reported previously in diatoms (Bailleul et al., 2015; Flori et al.,  
650 2017). Whether such contact sites occur and are functional in plants is unknown; however,  
651 these mechanisms are hypothesized to exist since it is necessary that chloroplasts exchange  
652 metabolites with mitochondria and peroxisomes to ensure activation of photorespiration  
653 concomitantly with photosynthesis. The study of membrane contact sites is an emerging field  
654 in cell biology (Scorrano et al., 2019). Future work will focus on analysing the dynamics and  
655 functionality of contact sites between chloroplast membranes and other organelles, and  
656 investigate the general coordination of plant cell metabolism during de-etiolation. These  
657 questions could be further addressed using the SBF-SEM stacks and proteomic resource  
658 described here.

659

## 660 **Materials and methods**

661

### 662 *Plant material and Growth conditions*

663 *Arabidopsis thaliana* seeds (Columbia ecotype) were surface-sterilized with 70% (v/v) ethanol  
664 with 0.05% (v/v) Triton X-100, then washed with 100% ethanol. Seeds were sown on agar  
665 plates containing 0.5 × Murashige and Skoog salt mixture (Duchefa Biochemie, Haarlem,  
666 Netherlands) without sucrose. Following stratification in the dark for 3 days at 4°C, seeds were  
667 irradiated with 40 μmol m<sup>-2</sup> s<sup>-1</sup> for 2 h at 21°C and then transferred to the dark for 3 days growth  
668 at 21°C. Etiolated seedlings were collected in the dark (0 h of light; T0) and at selected time  
669 points (T4, T8, T12, T24, T48, T72, T96) upon continuous white light exposure (40 μmol m<sup>-2</sup> s<sup>-1</sup>  
670 at 21°C).

671

672 *Photosynthetic parameters*

673 Maximum quantum yield of photosystem II ( $\Phi_{MAX} = F_v/F_M = (F_m - F_o)/F_m$  where  $F_m$  is the maximal  
674 fluorescence in dark adapted state,  $F_o$  is minimal fluorescence in dark adapted state,  $F_v$  is the  
675 variable fluorescence ( $F_m - F_o$ )), photosystem II quantum yield in the light ( $\Phi_{PSII}$ ), and  
676 photochemical quenching (qP) were determined using a Fluorcam (Photon Systems  
677 Instruments) with blue-light LEDs (470 nm). Plants were dark adapted for a minimum of 5 min  
678 before measurement.

679

680 *Chlorophyll concentration*

681 Chlorophylls were extracted in 4 volumes of dimethylformamide (DMF) (v/w) overnight at 4°C.  
682 After centrifugation, chlorophylls were measured using a NanoDrop™ instrument at 647 nm  
683 and 664 nm. Chlorophyll contents were calculated according to previously described methods  
684 (Porra et al., 1989).

685

686 *Transmission electron microscopy (TEM)*

687 Samples were fixed under vacuum (200 mBar) in 0.1 M cacodylate buffer (pH 7.4) containing  
688 2.5% (w/v) glutaraldehyde and 2% (w/v) formaldehyde (fresh from paraformaldehyde) for 4 h  
689 and left in the fixation solution for 16 h at 4°C. Samples were then incubated in a solution  
690 containing 3% (w/v) potassium ferrocyanide and 4 mM calcium chloride in 0.1 M cacodylate  
691 buffer combined with an equal volume of 4% (w/v) aqueous osmium tetroxide ( $OsO_4$ ) for 1 h,  
692 on ice. After the first heavy metal incubation, samples were rinsed with ddH<sub>2</sub>O and treated with  
693 1% (w/v) thiocarbohydrazide solution for 1 h at 60°C. Samples were rinsed (ddH<sub>2</sub>O for 15 min)  
694 before the second exposure to 2% (w/v)  $OsO_4$  aqueous solution for 30 min at room  
695 temperature. Following this second exposure to osmium, tissues were placed in 1% (w/v)  
696 uranyl acetate (aqueous) and left overnight at 4°C. The samples were rinsed with ddH<sub>2</sub>O for  
697 15 min, and placed in the lead aspartate solution for 30 min at 60°C. Samples were dehydrated  
698 in a series of aqueous ethanol solutions ranging from 50% (v/v) to 100%, then embedded in  
699 Durcupan resin by successive changes of Durcupan resin/acetone mixes, with the last  
700 imbibition in 100% Durcupan resin. Polymerization of the resin was conducted for 48 h at 60°C  
701 (Deerinck et al., 2010). Ultra-thin sections (70 nm) were cut using Ultrathin-E microtome  
702 (Reichert-Jung) equipped with a diamond knife. The sections were analysed with a Philips CM-  
703 100 electron microscope operating at 60 kV.

704

705 *Confocal microscopy*

706 To derive the chloroplast and cell volumes, images of 1–5- $\mu$ m thick sections of cotyledon cells  
707 were acquired with X10 and X40 oil immersion objectives using a LEICA TCS SP5 confocal

708 laser scanning microscope. Chlorophyll was excited using a red laser (33%) and spectral  
709 detection channel was PMT3.

710

711

712

### 713 *SBF-SEM*

714 SBF-SEM was performed on Durcupan resin–embedded cotyledons representing the four de-  
715 etiolation time points T0, T4, T24, and T96. Overview of the mesophyll tissue ( $\approx 600$  images)  
716 and zoomed stacks of the chloroplasts ( $\approx 300$  images) were acquired. Voxel size of T4 zoomed  
717 stacks: 3.9 x 3.9 x 50 nm; T24: 4.7 x 4.7 x 50 nm; T96: 5.6 x 5.6 x 50 nm. Voxel size for T0  
718 overview: 9.5 x 9.5 x 100 nm; T4: 19.3 x 19.3 x 100 nm; T24: 40 x 40 x 200 nm; T96: 43.5 x  
719 43.5 x 200 nm.

720 Acquired datasets were aligned and smoothed respectively, using the plugins MultiStackReg  
721 and 3D median filter, provided by the open-source software Fiji.

722 We performed a stack-reslice from Fiji to generate a new stack by reconstructing the slices at  
723 a new pixel depth to obtain isotropic voxel size and improve z-resolution. The segmentation  
724 and 3D mesh geometry information of plastid /thylakoid (T0, T4, T24 and T96) were  
725 implemented by open-source software 3D Slicer (Fedorov et al., 2012) and MeshLab (Cignoni  
726 et al., 2008) respectively.

727

### 728 *Segmentation, 3D reconstruction, and surface and volume quantification*

729 Segmentation and 3D reconstruction of 3View and confocal images were performed using  
730 Amira software (FEI Visualization Sciences Group). Specifically, prolamellar body, thylakoids,  
731 and envelope membranes as well as the cells were selected using a semi-automatic tool called  
732 Segmentation Editor. From the segmented images, triangulated 3D surfaces were created  
733 using Generate Surface package. Quantification of morphometric data (Area 3D and volume  
734 3D) was acquired using Label Analysis package.

735

### 736 *Analysis of grana segmentation*

737 Grana structures acquired from SBF-SEM were selected in Amira. The grana selections were  
738 converted in line set view in Amira software using the Generate Contour line package. To  
739 complete the grana segmentation, the line set views were imported into the Rhino 6 software  
740 (Robert McNeel & Associates, USA). Every granum was segmented in layers with a specific  
741 thickness and distance according to quantitative data collected (Figure 2- figure supplement 1  
742 and Figure 3- figure supplement 1). After segmentation, images were re-imported in Amira  
743 software to quantify perimeter using the Label Analysis package.

744

745 *Chloroplast number determination*

746 Chloroplasts per cell were counted manually using Image J software (Wayne Rasband,  
747 National Institutes of Health). From the same SBF-SEM stack, 5 and/or 6 cells were cropped  
748 at each time point (T0, T4, T24, and T96) to quantify chloroplast number per cell. From TEM  
749 images, chloroplast number/cell was determined at T24 (16 cells), T48 (12 cells), T72 (12  
750 cells), and T96 (17 cells). TEM images were acquired from two independent experiments.

751

752 *Liquid chromatography–mass spectrometry analysis and protein quantification*

753 Etiolated seedlings were grown as described above. At each time point, ca. 80 seedlings were  
754 pooled, frozen in liquid nitrogen, and stored at -80°C until use. Frozen material was ground  
755 with a mortar and pestle, and 40–80 mg of plant material was used for protein and peptide  
756 preparation using the iST kit for plant tissues (PreOmics, Germany). Briefly, each sample was  
757 resuspended in 100 µL of the provided ‘Lysis’ buffer and processed with High Intensity  
758 Focused Ultrasound (HIFU) for 1 min by setting the ultrasonic amplitude to 65% to enhance  
759 solubilization. For each sample, 100 µg of protein was transferred to the cartridge and digested  
760 by adding 50 µL of the provided ‘Digest’ solution. After 180 min of incubation at 37°C, the  
761 digestion was stopped with 100 µL of the provided ‘Stop’ solution. The solutions in the cartridge  
762 were removed by centrifugation at 3,800 g, whereas the peptides were retained on the iST  
763 filter. Finally, the peptides were washed, eluted, dried, and re-solubilized in 18.7 µL of solvent  
764 (3% (v/v) acetonitrile, 0.1% (v/v) formic acid).

765 Mass spectrometry (MS) analysis was performed on a Q Exactive HF-X mass spectrometer  
766 (Thermo Scientific) equipped with a Digital PicoView source (New Objective) and coupled to a  
767 M-Class UPLC (Waters). Solvent composition at the two channels was 0.1% (v/v) formic acid  
768 for channel A and 0.1% formic acid, 99.9% (v/v) acetonitrile for channel B. For each sample,  
769 2 µL of peptides were loaded on a commercial MZ Symmetry C18 Trap Column (100 Å, 5 µm,  
770 180 µm x 20 mm, Waters) followed by nanoEase MZ C18 HSS T3 Column (100 Å, 1.8 µm, 75  
771 µm x 250 mm, Waters). The peptides were eluted at a flow rate of 300 nL/min by a gradient of  
772 8–27% B in 85 min, 35% B in 5 min, and 80% B in 1 min. Samples were acquired in a  
773 randomized order. The mass spectrometer was operated in data-dependent mode (DDA),  
774 acquiring a full-scan MS spectra (350–1400 m/z) at a resolution of 120,000 at 200 m/z after  
775 accumulation to a target value of 3,000,000, followed by HCD (higher-energy collision  
776 dissociation) fragmentation on the 20 most intense signals per cycle. HCD spectra were  
777 acquired at a resolution of 15,000 using a normalized collision energy of 25 and a maximum  
778 injection time of 22 ms. The automatic gain control (AGC) was set to 100,000 ions. Charge  
779 state screening was enabled. Singly, unassigned, and charge states higher than seven were  
780 rejected. Only precursors with intensity above 250,000 were selected for MS/MS. Precursor  
781 masses previously selected for MS/MS measurement were excluded from further selection for

782 30 s, and the exclusion window was set at 10 ppm. The samples were acquired using internal  
783 lock mass calibration on m/z 371.1012 and 445.1200. The mass spectrometry proteomics data  
784 were handled using the local laboratory information management system (LIMS) (Türker et al.,  
785 2010).

786 Protein quantification based on precursor signal intensity was performed using ProgenesisQI  
787 for Proteomics (v4.0.6403.35451; nonlinear dynamics, Waters). Raw MS files were loaded into  
788 ProgenesisQI and converted to mzIn files. To select the alignment reference, a group of  
789 samples that had been measured in the middle of the run (to account for drifts in retention  
790 times) and derived from de-etiolation time point T12 or later (to account for increasing sample  
791 complexity) was preselected, from which replicate 3 of time point T48 was then automatically  
792 chosen as best alignment reference. After automatic peak picking, precursor ions with charges  
793 other than 2+, 3+, or 4+ were discarded. The five highest-ranked MS/MS spectra, at most, for  
794 each peptide ion were exported, using the deisotoping and charge deconvolution option and  
795 limiting the fragment ion count to 200 peaks per MS/MS. The resulting Mascot generic file  
796 (.mgf) was searched with Mascot Server version 2.6.2 ([www.matrixscience.com](http://www.matrixscience.com)) using the  
797 following settings: trypsin digest with up to two missed cleavages allowed;  
798 carbamidomethylation of cysteine as fixed modification; N-terminal acetylation and oxidation  
799 of methionine residue as variable modifications; precursor ion mass tolerance 10 ppm;  
800 fragment ion (MS/MS) tolerance 0.04 kDa. This search was performed against a forward and  
801 reverse (decoy) Araport11 database that included common MS contaminants and iRT  
802 peptides. The mascot result was imported into Scaffold Q+S (v4.8.9; Proteome Software Inc),  
803 where a spectrum report was created using a false discovery rate (FDR) of 10% and 0.5% at  
804 the protein and peptide level, respectively, and a minimum of one identified peptide per protein.  
805 After loading the spectrum report into ProgenesisQI, samples were normalized using the  
806 “normalize to all proteins” default settings (i.e. normalization was performed to all ions with  
807 charges 2+, 3+ or 4+). Samples were grouped according to de-etiolation time point in a  
808 between-group analysis with 4 replicates for each condition, except for time point T0 and T48,  
809 where n = 3. For these two time points, one replicate each had been discarded it appeared as  
810 an outlier in principal component analysis (PCA) of protein abundances between different runs  
811 (Supplemental dataset 1).. Quantification employed the Hi-N method, measuring the three  
812 most abundant peptides for each protein (Grossmann et al., 2010), and associated statistics  
813 (q-value, PCA etc.) were calculated in ProgenesisQI. Quantification also used protein  
814 grouping, which assigns proteins for which only shared but no unique peptides were identified  
815 to a ‘lead’ identifier containing all these shared peptides and thus having the greatest coverage  
816 among all grouped identifiers or highest score where coverage is equal. Quantification was  
817 restricted to protein (groups) with at least two identified peptides among which at least one is  
818 unique to the protein (group). Using these requirements, 5082 Arabidopsis proteins (or groups)



819 were identified. Since 13 additional identifications were exclusively associated with decoy  
820 proteins, the false discovery rate at the protein level is estimated to be 0.3% .

821

### 822 *Immunoblot analysis*

823 Proteins were extracted from whole seedlings in 4 volumes (w/v) of SDS-PAGE sample buffer  
824 (0.2 M Tris/HCL pH 6.8, 0.4 M dithiothreitol, 8% (w/v) SDS, 0.4% (w/v) Bromophenol blue, and  
825 40% (v/v) glycerol).

826 Proteins were denatured for 15 min at 65°C and cell debris were removed by centrifugation for  
827 5 min at 16,000 g. Proteins were separated on SDS-PAGE (10–15% (w/v) polyacrylamide  
828 concentrations depending on the molecular weight of the protein of interest) and transferred  
829 onto a nitrocellulose membrane for immunoblotting (overnight at 4°C) in Dunn buffer (10 mM  
830 NaHCO<sub>3</sub>, 3 mM Na<sub>2</sub>CO<sub>3</sub>, 0.01% (w/v) SDS, and 20% ethanol).

831 Absolute quantification of PsaA, PetC, and PsaC was performed according to Agrisera  
832 instructions and using recombinant proteins (PsaA AS01 0116S, PetC AS08 330S, and PsaC  
833 AS04 042S; Agrisera, Vännäs, SWEDEN). Three respective calibration curves for the three  
834 recombinant proteins were created. Concentrations used to generate the PsaA and PetC  
835 calibration curves were 1.75, 2.5, 5, and 10 (ng/μL). Concentrations used to generate the PsaC  
836 calibration curve were 0.375, 0.75, 1.5, and 3 (ng/μL). Immunodetections were performed  
837 using specific antibodies: anti-Actin (Sigma, A0 480) at 1/3,000 dilution in 5% (w/v) milk in Tris-  
838 buffered saline (TBS); anti-Lhcb2 (Agrisera, AS01 003), anti-D1(PsaA) (Agrisera, AS05 084),  
839 anti-PsaO (Agrisera, AS14 2825), anti-PsaD (Agrisera, AS06 146), anti-PetC (Agrisera, AS08  
840 330), and anti-AtpC (Agrisera, AS08 312) at 1/5,000 dilution in 5% milk/TBS; Anti-PsaD  
841 (Agrisera, AS09 461) at 1/2,000 in 5% milk/TBS; and anti-PsaC (Agrisera, AS042P) and anti-  
842 ARC5 (Agrisera, AS13 2676) at 1/2,000 in 3% (w/v) bovine serum albumin (BSA) in TBS. Anti-  
843 FtsZ-1 and anti-FtsZ2-1/FtsZ 2-2 (El-Shami et al., 2002; Karamoko et al., 2011) and were used  
844 at 1/2,000 dilution in 5% milk/TBS. After incubation with primary antibodies overnight at 4°C,  
845 blots were washed 3 times in TBS containing 0.1% (v/v) Tween without antibodies for 10  
846 minutes and incubated for 1 h at RT with horseradish peroxidase–conjugated secondary  
847 antibodies (1/3,000 (v/v) anti-rabbit or anti-mouse secondary antibodies, Agrisera).  
848 Chemiluminescence signals were generated with Enhanced chemiluminescence reagent (1 M  
849 Tris/HCl pH 8.5, 90 mM coumaric acid, and 250 mM luminol) and detected with a Fujifilm Image  
850 - Quant LAS 4000 mini CCD (GE Healthcare). Quantifications were performed with  
851 ImageQuant TL software (GE Healthcare).

852

### 853 *Lipid profiling*

854 Lipids were extracted from whole seedlings ground in a mortar and pestle under liquid nitrogen.  
855 Ground plant material corresponding to 40–80 mg fresh weight was suspended in

856 tetrahydrofuran:methanol (THF/MeOH) 50:50 (v/v). 10–15 glass beads (1 mm in diameter)  
857 were added followed by homogenization (3 min, 30 Hz,) and centrifugation (3 min, 14 000 g,  
858 at 4°C). The supernatant was removed and transferred to an HPLC vial. Lipid profiling was  
859 carried out by ultra-high pressure liquid chromatography coupled with atmospheric pressure  
860 chemical ionization-quadrupole time-of-flight mass spectrometry (UHPLC-APCI-QTOF-MS)  
861 (Martinis et al., 2011). Reverse-phase separation was performed at 60°C on an Acquity BEH  
862 C18 column (50 × 2.1 mm, 1.7 µm). The conditions were the following: solvent A = water;  
863 solvent B = methanol; 80–100% B in 3 min, 100% B for 2 min, re-equilibration at 80% B for 0.5  
864 min. Flow rate was 0.8 ml min<sup>-1</sup> and the injection volume 2.5 µl. Data were acquired using  
865 MassLynx version 4.1 (Waters), and processed with MarkerLynx XS (Waters). Peak lists  
866 consisting of variables described by mass-to-charge ratio and retention time were generated  
867 (Martinis et al., 2011; Spicher et al., 2016).

868 Absolute quantification of mono- (MGDG) and di-galactosyldiacylglycerol (DGDG) was  
869 conducted by creating calibration curves using MGDG (reference number 840523) and DGDG  
870 (reference number 840523) products of Avanti Company. Calibration curves were prepared  
871 using the following concentrations: 0.08, 0.4, 2, 10, and 50 µg ml<sup>-1</sup> of MGDG or DGDG.

872

873

#### 874 *Mathematical Model*

875 A non-linear mixed effects model (with fixed effect of time and random effect of replicates on  
876 3 of the parameters), built on a 4-parameter logistic function, was implemented in R (free  
877 software created by Ross Ihaka and Robert Gentleman, Auckland University, New Zealand),  
878 following the examples in Pinheiro and Bates (2000). The R-packages used are: nlme  
879 (Pinheiro and Bates, 2000), effects, lattice and car (Fox and Weisberg, 2018). To account for  
880 self-correlation at the replicate level, we proceeded to fit an overall mixed-effects model to the  
881 data (package 'nlme' from R), using the replicate's as random effect term (Figure  
882 9\_supplement 1). The four parameters *a*, *b*, *c* and *d* have been calculated (Figure  
883 9\_supplement 1) and the three plots (one for each biological replicate) (Figure 9\_supplement  
884 1) indicated the fitting curve for a series of data points.

885

#### 886 **Acknowledgements**

887 This work was supported by the University of Neuchâtel and ETH Zurich, a grant from the  
888 Swiss National Science Foundation (3100A0-112638) to E.D., and grants 31003A\_156998 and  
889 31003A\_176191 to F.K.. We thank Jonas Grossmann, Laura Kunz and Paolo Nanni from the  
890 Functional Genomic Center Zurich (FGCZ) for peptide preparation for mass spectrometry,  
891 acquisition of the raw data and help with associated data analysis, the ETH Zurich microscopy

892 facility (ScopeM) for advice in conducting SBF-SEM analysis. We thank Slobodeanu Radu  
893 Alexandru and Federico Giacomarra for help with bioinformatics analysis, and Romain Bessire  
894 for help with image processing software. We thank Roman Ulm and Michel Goldschmidt-  
895 Clermont for critical reading of the manuscript.

896

#### 897 **Author contributions**

898 Conceptualization, R.P., T.P., S.Z., F.K., and E.D.; Investigation, R.P., S.E., B.P., D.F., C.U.,  
899 G.G., and E.D.; Writing R.P, B.P., F.K. and E.D.; Supervision, F.K. and E.D.

900

#### 901 **Competing interests**

902 The authors declare no competing interests.

903

#### 904 **Figure Legends**

905 **Figure 1: Photosynthesis onset during de-etiolation.** (A) Scheme of the experimental  
906 design. Seeds of *Arabidopsis thaliana* (Columbia) sown on agar plates were stratified for three  
907 days at 4°C and then transferred to 22°C in the dark. After three days, etiolated seedlings were  
908 exposed to continuous white light (40  $\mu\text{mol}/\text{m}^2/\text{s}$ ) and harvested at different time points during  
909 de-etiolation. Selected time points used for different analyses are indicated. (B) Cotyledon  
910 phenotype of etiolated seedlings (T0) after 4 h (T4), 24 h (T24), and 96 (T96) h in continuous  
911 white light. Scale bars: 0.5 mm. (C) Chlorophyll quantification at different time points upon  
912 illumination. Error bars indicate  $\pm$  SD (n=3). (D) Maximum quantum yield of photosystem II  
913 (Fv/Fm). Error bars indicate  $\pm$  SD (n=4–10). For some data points, the error bars are inferior  
914 to the size of the symbol. Measurements of further photosynthetic parameters are presented  
915 in Figure 1- figure supplement 1.

916

#### 917 **Figure 2: Qualitative analysis of chloroplast ultrastructure during de-etiolation.**

918 Transmission electron microscopy (TEM) images of cotyledon cells of 3-day-old, dark-grown  
919 *Arabidopsis thaliana* (Columbia) seedlings illuminated for 0 h (A and E), 4 h (B and F), 24 h (C  
920 and G), and 96 h (D and H) in continuous white light (40  $\mu\text{mol}/\text{m}^2/\text{s}$ ). (A–D) Scale bars: 500  
921 nm, (E–H) higher magnification of A–D images; Scale bars: 200 nm. PLB: prolamellar body;  
922 PT: prothylakoid; PE: plastid envelope; SG: starch grain; GS: grana stack; SL: single lamella.  
923 Specific details for measurements of lamella thickness are provided in Figure 2- figure  
924 supplement 1.

925

#### 926 **Figure 3: 3D reconstructions of chloroplast thylakoid network during de-etiolation.** (A–

927 D) Scanning electron microscopy (SEM) micrographs of representative etioplasts and

928 chloroplasts from 3-day-old, dark-grown *Arabidopsis thaliana* seedlings illuminated for 0 h (T0;  
929 A), 4 h (T4; B), 24 h (T24; C), and 96 h (T96; D) in continuous white light (40  $\mu\text{mol}/\text{m}^2/\text{s}$ ). (E–  
930 H) Partial 3D reconstruction of thylakoid membranes (green) and envelope (blue) at T0 (E), T4  
931 (F), T24 (G) and T96 (H). Z-depth of thylakoid membrane reconstruction corresponds to 0.06  
932  $\mu\text{m}$  (E), 0.10  $\mu\text{m}$  (F), 0.13  $\mu\text{m}$  (G), and 0.15  $\mu\text{m}$  (H). (I–N). 3D reconstruction of a thylakoid  
933 membrane of an etioplast at T0 (I) or a chloroplast at T4 (L), T24 (M), and T96 (N). Scale bars  
934 = 1  $\mu\text{m}$ . Details of grana segmentation at T24 are provided in Figure 3- figure supplement 1.  
935

936 **Figure 4: Quantitative analysis of chloroplast volume and thylakoid surface during de-**  
937 **etioloation.** Quantification of thylakoid surface per chloroplast (A) and chloroplast volume (B)  
938 using 3-day-old, dark-grown *Arabidopsis thaliana* (Columbia) seedlings illuminated for 0 h, 4  
939 h, 24 h, and 96 h in continuous white light (40  $\mu\text{mol}/\text{m}^2/\text{s}$ ). Morphometric data were quantified  
940 by Labels analysis module of Amira software. Error bars indicate  $\pm$  SD (n=3). The total  
941 thylakoid surface indicated in A corresponds to the thylakoid surface exposed to the stroma,  
942 calculated in Amira software, in addition to the percentage of the grana surface (%Gs)  
943 calculated as described in Figure 3- figure supplement 1.  
944

945 **Figure 5: Accumulation dynamics of plastid proteins during de-etiolation.** 3-day-old  
946 etiolated seedlings of *Arabidopsis thaliana* were illuminated for 0 h (T0), 4 h (T4), 8 h (T8), 12  
947 h (T12), 24 h (T24), 48 h (T48), 72 h (T72), and 96 h (T96) under white light (40  $\mu\text{mol}/\text{m}^2/\text{s}$ ).  
948 Hierarchical clustering (Euclidean, average linkage) of normalized protein abundance for  
949 photosynthesis-(A), galactolipid metabolism- (B), chlorophyll metabolism- (C), and protein  
950 import-related proteins during de-etiolation (D). Protein abundance was quantified by shot-gun  
951 proteomics and heatmap colors indicate the fold change (average of 3–4 replicates) of each  
952 selected protein at each time point of de-etiolation (T0 to T96), relative to the last time point  
953 (T96). Note that some PORA values in panel D were higher than 3.5 and outside of the color  
954 range limits. Further hierarchical clustering based on the accumulation dynamics of all plastid-  
955 localized proteins is provided in Figure 5- figure supplement 1.  
956

957 **Figure 6: Accumulation dynamics of photosynthesis-related proteins during de-**  
958 **etioloation.** 3-day-old etiolated seedlings of *Arabidopsis thaliana* were illuminated for 0 h (T0),  
959 4 h (T4), 8 h (T8), 12 h (T12), 24 h (T24), 48 h (T48), 72 h (T72), and 96 h (T96) under white  
960 light (40  $\mu\text{mol}/\text{m}^2/\text{s}$ ). (A) Proteins were separated by SDS-PAGE and transferred onto  
961 nitrocellulose membrane and immunodetected with antibodies against PsbA, PsbD, PsbO,  
962 PetC, PsaD, PsaC, Lhcb2, AtpC, ELIP, POR proteins. (B–C) Quantification of PsbA, PetC,  
963 and PsaC during de-etiolation. Heatmap (B) was generated after normalization of the amount  
964 of each protein relative to the last time point (T96). Graph (C) corresponds to the absolute

965 quantification of proteins at T96. Error bars indicate  $\pm$  SD (n=3). Quantification of photosystem-  
966 related proteins during de-etiolation is detailed in Figure 6- figure supplement 1.

967

968 **Figure 7: Accumulation dynamics of galactolipids during de-etiolation.** 3-day-old  
969 etiolated seedlings of *Arabidopsis thaliana* were illuminated for 0 h (T0), 4 h (T4), 8 h (T8), 12  
970 h (T12), 24 h (T24), 48 h (T48), 72 h (T72), and 96 h (T96) under white light (40  $\mu\text{mol}/\text{m}^2/\text{s}$ ).  
971 (A) Heatmap representation of galactolipids (MGDG and DGDG) during de-etiolation. Samples  
972 were normalized to the last time point (T96). (B) Absolute quantification at T96 expressed in  
973 nmol/seedling. Error bars indicate  $\pm$  SD (n=4). (C) Absolute quantification (nmol/seedling) of  
974 the most abundant chloroplast galactolipids MGDG (MGDG 18:3/18:3, MGDG 18:3/16:3,  
975 MGDG 18:3/16:1) and DGDG (DGDG 18:3/18:3, DGDG 18:3/16:0) at different time points  
976 during de-etiolation. Error bars indicate  $\pm$  SD (n=4). (D) The MGDG/DGDG ratio was calculated  
977 using all 12 species of galactolipids detected during de-etiolation. Error bars indicate  $\pm$  SD  
978 (n=4).

979

980

981 **Figure 8: Relationship between chloroplast proliferation and chloroplast volume.** (A-B)  
982 Chloroplast number and cell volume in cotyledons of 3-day-old, dark-grown *Arabidopsis*  
983 *thaliana* seedlings illuminated for 0 h (T0), 4 h (T4), 24 h (T24), and 96 h (T96) in continuous  
984 white light (40  $\mu\text{mol}/\text{m}^2/\text{s}$ ). (A) Chloroplast number per cell during de-etiolation. Error bars  
985 indicate  $\pm$  SD (n=6 for T0 and T7; 7 for T24; 5 for T96). (B) Cell volume was quantified by the  
986 Labels analysis module of Amira software. Error bars indicate  $\pm$  SD (n=5–6). (C–D) Total  
987 proteins were extracted from T0–T96 seedlings, separated on SDS-PAGE, and transferred  
988 onto nitrocellulose. Proteins involved in plastid division (C, FtsZ; D, ARC5) and loading control  
989 (actin) were detected using specific antibodies (FtsZ2 antibody recognizes both FtsZ2-1 and  
990 FtsZ2-2). (E) Volume of dividing chloroplast at T24 and T96. Error bars indicate  $\pm$  SD (n=3).  
991 Further details of chloroplast proliferation in parallel with cell expansion are provided in Figure  
992 8- figure supplement 1.

993

994

995 **Figure 9: Superimposition of thylakoid surface per seedling obtained from**  
996 **morphometric analysis and mathematical modeling.** Thylakoid surface per seedling was  
997 estimated using quantitative data from 3View analysis ('MORPHO' black dots at T4, T24, and  
998 T96; and see Figure 4 and Table 1) and model generated using the quantitative data from  
999 proteomics and lipidomics ('MODEL' red line at T0, T4, T8, T12, T24, T48, T72, and T96, and  
1000 Table 1). Further details are provided in Figure 9- figure supplement 1 and 2.

1001

1002 **Figure 10: Overview of changes observed during the de-etiolation process**  
1003 **in *Arabidopsis thaliana* seedlings.** The 'Structure Establishment Phase' is correlated with  
1004 disassembly of the PLB and gradual formation of the thylakoid membrane as well as an initial  
1005 increase of eukaryotic (after 8 h) and prokaryotic (after 24 h) galactolipids and photosynthesis-  
1006 related proteins (PSII subunits at 4 h, PSI and cyt *b<sub>6</sub>f* at 12 h). The subsequent 'Chloroplast  
1007 Proliferation Phase' is associated with an increase in chloroplast number in concomitance with  
1008 cell expansion, a linear increase of prokaryotic and eukaryotic galactolipids and  
1009 photosynthesis-related proteins, and increased grana stacking. The red curve (retrieved from  
1010 the Figure 9) shows thylakoid surface/seedling dynamics during the de-etiolation process.

1011

1012

1013 **TABLE 1: Collection of quantitative data.** Morphometric data corresponding to thylakoid  
1014 surfaces and volumes, thylakoid/envelope surface ratio, and chloroplast and cell volumes were  
1015 collected after 3View analysis. Chloroplast and cell volumes were also quantified by  
1016 subsequent confocal microscopy analysis, whereas plastid length was measured using TEM  
1017 images. Molecular data for galactolipids (GLs) were analysed by lipidomics, whereas PsbA,  
1018 PsaC, and PetC were quantified by quantitative immunodetection.

1019

1020 **TABLE 2: Surface area occupied by the main galactolipids (MGDG and DGDG) and**  
1021 **photosynthetic complexes (PSII, cyt *b<sub>6</sub>f*, and PSI).** Shown are values at different time points  
1022 following illumination of 3-day-old etiolated seedlings. Each value (in bold) indicates the  
1023 calculated surface area in  $\mu\text{m}^2$  and corresponds to the average of three biological replicates.  
1024 Errors indicate SD.

1025

1026 **TABLE 3: Surface area occupied by galactolipid and photosynthetic complexes.** (A)  
1027 Values were retrieved from the corresponding references. MGDG and DGDG surfaces  
1028 correspond to the minimal molecular area. The surfaces of PSII-LHCII, PSI, and Cyt *b<sub>6</sub>f*  
1029 complexes correspond to the surface exposed to the stroma (19\*26 nm, 20\*15 nm, and 90\*55  
1030 Å, respectively). (B) Values from the table in panel A were used to calculate the total surface  
1031 per seedling corresponding to MGDG and DGDG galactolipids, and PSII, PSI, and Cyt *b<sub>6</sub>f*  
1032 complexes.

1033

1034

1035

1036

## 1037 Figure Supplements

### 1038 **Figure 1- figure supplement 1: Photosynthesis parameters during de-etiolation.**

1039 Maximum photosynthetic quantum yield of PSII (Fv/Fm) of plants (dark-adapted for 5 minutes)  
1040 grown under different light intensities (A). Photochemical quenching (B) and efficiency of the  
1041 photosystem PSII ( $\Phi$  PSII; C) measurements were made on 3-day-old etiolated seedlings that  
1042 were de-etiolated under continuous light (40  $\mu\text{mol}/\text{m}^2/\text{s}$ ) using a Fluorcam (Photon System  
1043 Instrument). Error bars indicate  $\pm$  SD (n=10).

1044  
1045 **Figure 2- figure supplement 1: Measurement of lamella thickness.** (A) TEM chloroplast  
1046 micrographs of 3-day-old, dark-grown *Arabidopsis thaliana* (Columbia) seedlings illuminated  
1047 for 96 h in continuous white light (40  $\mu\text{mol}/\text{m}^2/\text{s}$ ) were used to measure the thickness of  
1048 lamellae that constitute the grana stack. Measurements were performed using ImageJ. Scale  
1049 bar: 100 nm. (B) Equation used to calculate the thickness of one lamella. (C) Data indicate  
1050 mean  $\pm$  SD (n=10 for 2 lamellae and n=7 for 3 lamellae).

1051  
1052 **Figure 4- figure supplement 1: Grana segmentation (T24).** (A) Selection of thylakoid  
1053 membrane exposed to the stroma was acquired using Amira. (B) The perimeter of the grana  
1054 structures showed in black were segmented in layers of a specific thickness and distance using  
1055 Rhino software, with the corresponding thickness (lamellae and stromal gap) measured and  
1056 calculated as described in Figure 2- figure supplement 1. Grana segmentation was performed  
1057 using thylakoid membrane of de-etiolating seedlings exposed to continuous white light (40  
1058  $\mu\text{mol}/\text{m}^2/\text{s}$ ) for 24 (T24) and 96 (T96) h. A representative example of a T24 replicate is  
1059 illustrated here. (C) Schematic representation of the grana stack perimeter comprising  
1060 margins, end membranes, and intergranal lamellae. (D) Equation used to calculate the  
1061 percentage of the grana stack surface area relative to total thylakoid surface area.

1062  
1063 **Figure 5- figure supplement 1: Accumulation dynamics of selected plastid proteins**  
1064 **during de-etiolation.** Hierarchical clustering (Euclidean, average linkage) of normalized  
1065 protein abundance (log2 fold changes) for plastid-localized proteins during de-etiolation.  
1066 Normalization was performed to the last time point (96 h). Defined clusters are indicated with  
1067 different colours (1= purple; 2= pink; 3=turquoise; 4= brown; 5 = light green; 6 = dark green).  
1068 Protein IDs (AGI) and names are legible upon zoom-in.

1069  
1070 **Figure 6- figure supplement 1: Quantification of photosynthesis-related proteins.** (A)  
1071 Immunodetection of PsbA, PetC, and PsaC during de-etiolation. Dilutions were used for the  
1072 later time points to avoid saturation of the signal. (B) Different bands were detected by  
1073 Amersham Imager program and quantified by Image QuantTL (Amersham). (C) Calibration

1074 curves were created using recombinant proteins (Agrisera). Calibration curve composition:  
1075 PsbA 10 ng (A; lane a), 5 ng (b), 2.5 ng (c), and 1.25 ng (d); PetC 10 ng (e), 5 ng (f), 2.5 ng  
1076 (g), and 1.25 ng (h); PsaC 3 ng (i), 1.5 ng (l), 0.75 ng (m), and 0.325 ng (n). The analysis was  
1077 carried out on 3–4 independent experiments (BIO1–4).

1078  
1079 **Figure 8- figure supplement 1. Chloroplast proliferation in parallel with cell expansion.**

1080 SEM micrographs of 3-day-old, dark-grown *Arabidopsis thaliana* (Columbia) seedlings  
1081 illuminated for 0 h (T0; A), 4 h (T4; B), 24 h (T24; C), and 96 h (T96; D) in continuous white  
1082 light (40  $\mu\text{mol}/\text{m}^2/\text{s}$ ). Palisade (PA) and spongy (SP) cells are indicated. Scale bars: 15  $\mu\text{m}$ .  
1083 (E) 3D reconstruction of a palisade cell at T24 after segmentation of chloroplasts and cell  
1084 plasma membrane. (F–I) Confocal images of cotyledons of dark-grown seedlings at T24 (F),  
1085 T48 (G), T72 (H), and T96 (I). Scale bars: 10  $\mu\text{m}$ . (L–O) TEM micrographs of cotyledon cells  
1086 of dark-grown seedlings at T24 (L), T48 (M), T72 (N), and T96 (O). L–M, scale bars: 2  $\mu\text{m}$ ; N–  
1087 O, scale bars: 5  $\mu\text{m}$ . (P) Cell perimeter measured with Amira software using (red line). The Z-  
1088 depth of each stack corresponds to 1  $\mu\text{m}$ . Relative chloroplast number per cell was counted  
1089 using 2D TEM images (black line). Red error bars indicate  $\pm$  SD ( $n=17$ ). Black error bars  
1090 indicate  $\pm$  SD ( $n=3-4$ ). (Q) Box plots of single chloroplast total volume quantified at T48 and  
1091 T72. Each box corresponds to the distribution of a chloroplast population analysed using  
1092 confocal and SBF-SEM stacks.  $n=66$  (T48); 62 (T72).

1093

1094  
1095 **Figure 9- figure supplement 1: Non-linear mixed effect model of thylakoid surface**

1096 **during de-etiolation.** (A) Total surface of thylakoid membrane components (in  $\mu\text{m}^2$ ) in function  
1097 of de-etiolation time point. (B) Individual plots for each biological replicate. (C) Values, standard  
1098 errors, t-value, and P-value of the four parameters (a, b, c, and d) used in the main equation.

1099  $S_{\text{model}}$  = surface of thylakoid at a specific time (t)

1100 t = time of light exposure (h)

1101 a = asymptote (to the left if  $c > 0$ )

1102 b = right asymptote (to the right if  $c > 0$ )

1103 c = proportional to the slope of the curve at the inflection point

1104 d = inflection point (point at which the mean  $S_{\text{model}}$  value is reached)

1105

1106  
1107 **Figure 9- figure supplement 2: Morphometric analysis of cotyledons.** (A) Cotyledon

1108 surface area of 3-day-old, dark-grown *Arabidopsis thaliana* (Columbia) seedlings illuminated  
1109 with 24 h (T24) and 96 h (T96) of continuous white light (40  $\mu\text{mol}/\text{m}^2/\text{s}$ ). (B) The thickness (T)



1110 of mesophyll tissue constituted of palisade (PA), spongy (SP) cells, and vascular system (VS)  
1111 in addition to the epidermal tissue was measured. Error bars indicate  $\pm$  SD (n=4). (C)  
1112 Estimation of cotyledon volume. Error bars indicate  $\pm$  SD (n=3). (D) Estimation of the number  
1113 of cells per cotyledon (see Supplemental Dataset 4 for calculations)  
1114  
1115

## 1116 References

- 1117 Agne B, Kessler F. 2010. Modifications at the A-domain of the chloroplast import receptor  
1118 Toc159. *Plant Signal Behav* **5**:1513–6. doi:10.1104/pp.110.158048
- 1119 Amunts A, Nelson N. 2009. Plant Photosystem I Design in the Light of Evolution. *Structure*  
1120 **17**:637–650. doi:10.1016/j.str.2009.03.006
- 1121 Armarego-Marriott T, Kowalewska Ł, Burgos A, Fischer A, Thiele W, Erban A, Strand D,  
1122 Kahlau S, Hertle A, Kopka J, Walther D, Reich Z, Schöttler MA, Bock R. 2019. Highly  
1123 Resolved Systems Biology to Dissect the Etioplast-to-Chloroplast Transition in Tobacco  
1124 Leaves. *Plant Physiol* **180**:654–681. doi:10.1104/pp.18.01432
- 1125 Aronsson H, Schöttler M a, Kelly A a, Sundqvist C, Dörmann P, Karim S, Jarvis P. 2008.  
1126 Monogalactosyldiacylglycerol deficiency in Arabidopsis affects pigment composition in  
1127 the prolamellar body and impairs thylakoid membrane energization and photoprotection  
1128 in leaves. *Plant Physiol* **148**:580–592. doi:10.1104/pp.108.123372
- 1129 Austin JR, Staehelin LA. 2011. Three-Dimensional Architecture of Grana and Stroma  
1130 Thylakoids of Higher Plants as Determined by Electron Tomography. *Plant Physiol*  
1131 **155**:1601–1611. doi:10.1104/pp.110.170647
- 1132 Bailleul B, Berne N, Murik O, Petroutsos D, Prihoda J, Tanaka A, Villanova V, Bligny R, Flori  
1133 S, Falconet D, Krieger-Liszkay A, Santabarbara S, Rappaport F, Joliot P, Tirichine L,  
1134 Falkowski PG, Cardol P, Bowler C, Finazzi G. 2015. Energetic coupling between plastids  
1135 and mitochondria drives CO<sub>2</sub> assimilation in diatoms. *Nature* **524**:366–369.  
1136 doi:10.1038/nature14599
- 1137 Bastien O, Botella C, Chevalier F, Block MA, Jouhet J, Breton C, Girard-Egrot A, Maréchal E.  
1138 2016. New Insights on Thylakoid Biogenesis in Plant Cells, *International Review of Cell*  
1139 *and Molecular Biology*. Academic Press. doi:10.1016/bs.ircmb.2015.12.001
- 1140 Bauer J, Chen K, Hiltbunner a, Wehrli E, Eugster M, Schnell D, Kessler F. 2000. The major  
1141 protein import receptor of plastids is essential for chloroplast biogenesis. *Nature* **403**:203–  
1142 7. doi:10.1038/35003214
- 1143 Bischof S, Baerenfaller K, Wildhaber T, Troesch R, Vidi P-A, Roschitzki B, Hirsch-Hoffmann  
1144 M, Hennig L, Kessler F, Gruissem W, Baginsky S. 2011. Plastid proteome assembly  
1145 without Toc159: photosynthetic protein import and accumulation of N-acetylated plastid  
1146 precursor proteins. *Plant Cell* **23**:3911–28. doi:10.1105/tpc.111.092882

- 1147 Biswal B, Krupinska K, Biswal U. 2013. Plastid Development in Leaves during Growth and  
1148 Senescence. doi:10.1007/978-94-007-5724-0
- 1149 Block MA, Dorne A-J, Joyard J, Douce R. 1983. Preparation and Characterization of  
1150 Membrane Fractions of Outer and Inner Envelope Membranes from Spinach C. *J Biol*  
1151 *Chem* **258**:13281–13286. doi:10.1007/978-94-017-4973-2\_5
- 1152 Blomqvist LA, Ryberg M, Sundqvist C. 2008. Proteomic analysis of highly purified prolamellar  
1153 bodies reveals their significance in chloroplast development. *Photosynth Res* **96**:37–50.  
1154 doi:10.1007/s11120-007-9281-y
- 1155 Bottier C, Géan J, Artzner F, Desbat B, Pézolet M, Renault A, Marion D, Vié V. 2007.  
1156 Galactosyl headgroup interactions control the molecular packing of wheat lipids in  
1157 Langmuir films and in hydrated liquid-crystalline mesophases. *Biochim Biophys Acta*  
1158 **1768**:1526–1540. doi:10.1016/j.bbamem.2007.02.021
- 1159 Bräutigam A, Weber APM. 2009. Proteomic analysis of the proplastid envelope membrane  
1160 provides novel insights into small molecule and protein transport across proplastid  
1161 membranes. *Mol Plant* **2**:1247–1261. doi:10.1093/mp/ssp070
- 1162 Caffarri S, Tibiletti T, Jennings R, Santabarbara S. 2014. A Comparison Between Plant  
1163 Photosystem I and Photosystem II Architecture and Functioning. *Curr Protein Pept Sci*  
1164 **15**:296–331. doi:10.2174/1389203715666140327102218
- 1165 Chen Y-E, Ma J, Wu N, Su Y-Q, Zhang Z-W, Yuan M, Zhang H-Y, Zeng X-Y, Yuan S. 2018.  
1166 The roles of Arabidopsis proteins of Lhcb4, Lhcb5 and Lhcb6 in oxidative stress under  
1167 natural light conditions. *Plant Physiol Biochem* **130**:267–276.  
1168 doi:<https://doi.org/10.1016/j.plaphy.2018.07.014>
- 1169 Cignoni P, Callieri M, Corsini M, Dellepiane M, Ganovelli F, Ranzuglia G. 2008. MeshLab: An  
1170 open-source mesh processing tool. *6th Eurographics Ital Chapter Conf 2008 - Proc* 129–  
1171 136. doi:10.2312/LocalChapterEvents/ItalChap/ItalianChapConf2008/129-136
- 1172 Daum B, Kühlbrandt W. 2011. Electron tomography of plant thylakoid membranes. *J Exp Bot*  
1173 **62**:2393–2402. doi:10.1093/jxb/err034
- 1174 Daum B, Nicastro D, McIntosh JR, Ku W. 2010. Arrangement of Photosystem II and ATP  
1175 Synthase in Chloroplast Membranes of Spinach and Pea 1299–1312.  
1176 doi:10.1105/tpc.109.071431

- 1177 Deerinck TJ, Bushong EA, Thor A, Ellisman MH. 2010. NCMIR methods for 3D EM: a new  
1178 protocol for preparation of biological specimens for serial block face scanning electron  
1179 microscopy 6–8.
- 1180 Demarsy E, Lakshmanan AM, Kessler F. 2014. Border control: selectivity of chloroplast protein  
1181 import and regulation at the TOC-complex. *Front Plant Sci* **5**:483.  
1182 doi:10.3389/fpls.2014.00483
- 1183 Demé B, Cataye C, Block M a, Maréchal E, Jouhet J. 2014. Contribution of galactoglycerolipids  
1184 to the 3-dimensional architecture of thylakoids. *FASEB J* **28**:3373–83. doi:10.1096/fj.13-  
1185 247395
- 1186 Dubreuil C, Jin X, Barajas-López J de D, Hewitt TC, Tanz SK, Dobrenel T, Schröder WP,  
1187 Hanson J, Pesquet E, Grönlund A, Small I, Strand \r Asa. 2018. Establishment of  
1188 Photosynthesis through Chloroplast Development Is Controlled by Two Distinct  
1189 Regulatory Phases. *Plant Physiol* **176**:1199–1214. doi:10.1104/pp.17.00435
- 1190 El-Shami M, El-Kafafi S, Falconet D, Lerbs-Mache S. 2002. Cell cycle-dependent modulation  
1191 of FtsZ expression in synchronized tobacco BY2 cells. *Mol Genet Genomics* **267**:254–  
1192 261. doi:10.1007/s00438-002-0660-y
- 1193 Engel BD, Schaffer M, Cuellar LK, Villa E, Plitzko JM, Baumeister W. 2015. Native architecture  
1194 of the chlamydomonas chloroplast revealed by in situ cryo-electron tomography. *Elife*  
1195 **2015**:1–29. doi:10.7554/eLife.04889
- 1196 Fedorov A, Beichel R, Kalpathy-Cramer J, Finet J, Fillion-Robin J-C, Pujol S, Bauer C,  
1197 Jennings D, Fennessy F, Sonka M, Buatti J, Aylward S, Miller J V, Pieper S, Kikinis R.  
1198 2012. 3D Slicer as an image computing platform for the Quantitative Imaging Network.  
1199 *Magn Reson Imaging* **30**:1323–1341. doi:https://doi.org/10.1016/j.mri.2012.05.001
- 1200 Ferro M, Salvi D, Brugière S, Miras S, Kowalski S, Louwagie M, Garin J, Joyard J, Rolland N.  
1201 2003. Proteomics of the chloroplast envelope membranes from *Arabidopsis thaliana*. *Mol*  
1202 *Cell Proteomics* **2**:325–345. doi:10.1074/mcp.M300030-MCP200
- 1203 Flori S, Jouneau P-H, Bailleul B, Gallet B, Estrozi LF, Moriscot C, Bastien O, Eicke S, Schober  
1204 A, Bártulos CR, Maréchal E, Kroth PG, Petroustos D, Zeeman S, Breyton C, Schoehn G,  
1205 Falconet D, Finazzi G. 2017. Plastid thylakoid architecture optimizes photosynthesis in  
1206 diatoms. *Nat Commun* **8**:15885. doi:10.1038/ncomms15885
- 1207 Fox J, Weisberg S. 2018. Visualizing fit and lack of fit in complex regression models with

- 1208 predictor effect plots and partial residuals, *Journal of Statistical Software*.  
1209 doi:10.18637/jss.v087.i09
- 1210 Grossmann J, Roschitzki B, Panse C, Fortes C, Barkow-Oesterreicher S, Rutishauser D,  
1211 Schlapbach R. 2010. One master protein that is identified by a set of peptides that are  
1212 not included (all together) in any other protein group. All proteins that are identified by the  
1213 same set or a subset of those peptides. *J Proteomics* **73**:1740–1746.  
1214 doi:doi:10.1016/j.jprot.2010.05.011
- 1215 Hashimoto M, Endo T, Peltier G, Tasaka M, Shikanai T. 2003. A nucleus-encoded factor,  
1216 CRR2, is essential for the expression of chloroplast ndhB in Arabidopsis. *Plant J* **36**:541–  
1217 549. doi:10.1046/j.1365-313X.2003.01900.x
- 1218 Hooper CM, Castleden IR, Tanz SK, Aryamanesh N, Millar AH. 2017. SUBA4: The interactive  
1219 data analysis centre for Arabidopsis subcellular protein locations. *Nucleic Acids Res*  
1220 **45**:D1064–D1074. doi:10.1093/nar/gkw1041
- 1221 Jouhet J, Marechal E, Block MA. 2007. Glycerolipid transfer for the building of membranes in  
1222 plant cells. *Prog Lipid Res* **46**:37–55. doi:10.1016/j.plipres.2006.06.002
- 1223 Karamoko M, El-Kafafi ES, Mandaron P, Lerbs-Mache S, Falconet D. 2011. Multiple FtsZ2  
1224 isoforms involved in chloroplast division and biogenesis are developmentally associated  
1225 with thylakoid membranes in Arabidopsis. *FEBS Lett* **585**:1203–1208.  
1226 doi:10.1016/j.febslet.2011.03.041
- 1227 Kato Y, Sakamoto W. 2018. FtsH protease in the thylakoid membrane: Physiological functions  
1228 and the regulation of protease activity. *Front Plant Sci* **9**:1–8. doi:10.3389/fpls.2018.00855
- 1229 Kessler F, Schnell DJ. 2006. The function and diversity of plastid protein import pathways: A  
1230 multilane GTPase highway into plastids. *Traffic* **7**:248–257. doi:10.1111/j.1600-  
1231 0854.2005.00382.x
- 1232 Kimura M, Manabe K, Abe T, Yoshida S, Matsui M, Yamamoto YY. 2003. Analysis of Hydrogen  
1233 Peroxide-independent Expression of the High-light-inducible ELIP2 Gene with the Aid of  
1234 the ELIP2 Promoter-Luciferase Fusion¶. *Photochem Photobiol* **77**:668–674.  
1235 doi:10.1562/0031-8655(2003)0770668AOHPEO2.0.CO2
- 1236 Kirchhoff H, Hall C, Wood M, Herbstová M, Tsabari O, Nevo R, Charuvi D, Eyal S, Ziv R. 2011.  
1237 Dynamic control of protein diffusion within the granal thylakoid lumen **108**:20248–20253.  
1238 doi:10.1073/pnas.1104141109

- 1239 Kleffmann T, von Zychlinski A, Russenberger D, Hirsch-Hoffmann M, Gehrig P, Gruissem W,  
1240 Baginsky S. 2007. Proteome Dynamics during Plastid Differentiation in Rice. *Plant*  
1241 *Physiol* **143**:912 LP – 923. doi:10.1104/pp.106.090738
- 1242 Kobayashi K. 2016. Role of membrane glycerolipids in photosynthesis, thylakoid biogenesis  
1243 and chloroplast development. *J Plant Res* **129**:565–580. doi:10.1007/s10265-016-0827-  
1244 y
- 1245 Koochak H, Puthiyaveetil S, Mullendore DL, Li M, Kirchhoff H. 2019. The structural and  
1246 functional domains of plant thylakoid membranes. *Plant J* **97**:412–429.  
1247 doi:10.1111/tpj.14127
- 1248 Kowalewska ŁM, Mazur R, Suski S, Garstka M, Mostowska A. 2016. Three-dimensional  
1249 visualization of the internal plastid membrane network during runner bean chloroplast  
1250 biogenesis. Dynamic model of the tubular-lamellar transformation. *Plant Cell* **28**:875–891.  
1251 doi:10.1105/tpc.15.01053
- 1252 Kubis S, Baldwin A, Patel R, Razzaq A, Dupree P, Lilley K, Kurth J, Leister D, Jarvis P. 2003.  
1253 The Arabidopsis ppi1 mutant is specifically defective in the expression, chloroplast import,  
1254 and accumulation of photosynthetic proteins. *Plant Cell* **15**:1859–1871.  
1255 doi:10.1105/tpc.012955
- 1256 Kurisu G, Zhang H, Smith JL, Cramer WA. 2003. Structure of the Cytochrome b 6 f Complex  
1257 of Oxygenic Photosynthesis: Tuning the Cavity **302**:1009–1015.  
1258 doi:10.1126/science.1090165
- 1259 Li XP, Björkman O, Shih C, Grossman AR, Rosenquist M, Jansson S, Niyogi KK. 2000. A  
1260 pigment-binding protein essential for regulation of photosynthetic light harvesting. *Nature*  
1261 **403**:391–395. doi:10.1038/35000131
- 1262 Liang Z, Zhu N, Mai KK, Liu Z, Tzeng D, Osteryoung KW. 2018. Thylakoid-Bound Polysomes  
1263 and a Dynamin-Related Protein, FZL, Mediate Critical Stages of the Linear Chloroplast  
1264 Biogenesis Program in Greening Arabidopsis Cotyledons **30**:1476–1495.  
1265 doi:10.1105/tpc.17.00972
- 1266 Marechal E, Block MA, Dome A, Douce R, Joyard J. 1997. Lipid synthesis and metabolism in  
1267 the plastid envelope **100**:65–77. doi:10.1111/j.1399-3054.1997.tb03455.x
- 1268 Martinis J, Kessler F, Glauser G. 2011. A novel method for prenylquinone profiling in plant  
1269 tissues by ultra-high pressure liquid chromatography-mass spectrometry. *Plant Methods*

- 1270 7:1–23. doi:10.1186/1746-4811-7-23
- 1271 Mazur R, Mostowska A, Szach J, Gieczewska K, Wójtowicz J, Bednarska K, Garstka M,  
1272 Kowalewska Ł. 2019. Galactolipid deficiency disturbs spatial arrangement of the thylakoid  
1273 network in *Arabidopsis thaliana* plants. *J Exp Bot* **70**:4689–4703. doi:10.1093/jxb/erz219
- 1274 Mi H, Muruganujan A, Huang X, Ebert D, Mills C, Guo X, Thomas PD. 2019. Protocol Update  
1275 for large-scale genome and gene function analysis with the PANTHER classification  
1276 system (v.14.0). *Nat Protoc* **14**:703–721. doi:10.1038/s41596-019-0128-8
- 1277 Michaud M, Jouhet J. 2019. Lipid Trafficking at Membrane Contact Sites During Plant  
1278 Development and Stress Response. *Front Plant Sci* **10**:1–10.  
1279 doi:10.3389/fpls.2019.00002
- 1280 Ohlrogge J, Browse J. 1995. Lipid biosynthesis. *Plant Cell* **7**:957–970. doi:10.1105/tpc.7.7.957
- 1281 Peddie CJ, Collinson LM. 2014. Exploring the third dimension: Volume electron microscopy  
1282 comes of age. *Micron* **61**:9–19. doi:10.1016/j.micron.2014.01.009
- 1283 Pinali C, Kitmitto A. 2014. Serial block face scanning electron microscopy for the study of  
1284 cardiac muscle ultrastructure at nanoscale resolutions. *Curr Ther Res - Clin Exp* **76**:1–  
1285 11. doi:10.1016/j.yjmcc.2014.08.010
- 1286 Pinheiro J, Bates M. 2000. Pinheiro - Mixed Effects Models in S & S PLUS. *Springer B.*  
1287 doi:org/10.1007/b98882
- 1288 Plöscher M, Reisinger V, Eichacker LA. 2011. Proteomic comparison of etioplast and  
1289 chloroplast protein complexes. *J Proteomics* **74**:1256–1265.  
1290 doi:10.1016/j.jprot.2011.03.020
- 1291 Porra RJ, Thompson WA, Kriedemann PE. 1989. Determination of accurate extinction  
1292 coefficients and simultaneous equations for assaying chlorophylls a and b extracted with  
1293 four different solvents: verification of the concentration of chlorophyll standards by atomic  
1294 absorption spectroscopy. *Biochim Biophys Acta - Bioenerg* **975**:384–394.  
1295 doi:https://doi.org/10.1016/S0005-2728(89)80347-0
- 1296 Pyke KA, Leech RM. 1994. A Genetic Analysis of Chloroplast Division and Expansion in  
1297 *Arabidopsis thaliana*. *Plant Physiol* **104**:201–207. doi:10.1104/pp.104.1.201
- 1298 Reiland S, Grossmann J, Baerenfaller K, Gehrig P, Nunes-nesi A. 2011. Integrated proteome  
1299 and metabolite analysis of the de-etiolation process in plastids from rice (*Oryza sativa*

- 1300 L.) **11**:1751–1763. doi:10.1002/pmic.201000703
- 1301 Richardson LGL, Schnell DJ. 2019. Origins, function, and regulation of the TOC–TIC general  
1302 protein import machinery of plastids. *J Exp Bot* **71**:1226–1238. doi:10.1093/jxb/erz517
- 1303 Rudowska L, Gieczewska K, Mazur R, Garstka M, Mostowska A. 2012. Chloroplast biogenesis  
1304 - correlation between structure and function. *Biochim Biophys Acta* **1817**:1380–7.  
1305 doi:10.1016/j.bbabi.2012.03.013
- 1306 Runge S, Sperling U, Frick G, Apel K, Armstrong GA. 1996. Distinct roles for light-dependent  
1307 NADPH:protochlorophyllide oxidoreductases (POR) A and B during greening in higher  
1308 plants. *Plant J* **9**:513–523. doi:10.1046/j.1365-313X.1996.09040513.x
- 1309 Scorrano L, De Matteis MA, Emr S, Giordano F, Hajnóczky G, Kornmann B, Lackner LL, Levine  
1310 TP, Pellegrini L, Reinisch K, Rizzuto R, Simmen T, Stenmark H, Ungermann C,  
1311 Schuldiner M. 2019. Coming together to define membrane contact sites. *Nat Commun*  
1312 **10**:1–11. doi:10.1038/s41467-019-09253-3
- 1313 Solymosi K, Schoefs B. 2010. Etioplast and etio-chloroplast formation under natural conditions:  
1314 The dark side of chlorophyll biosynthesis in angiosperms. *Photosynth Res* **105**:143–166.  
1315 doi:10.1007/s11120-010-9568-2
- 1316 Spicher L, Glauser G, Kessler F. 2016. Lipid Antioxidant and Galactolipid Remodeling under  
1317 Temperature Stress in Tomato Plants. *Front Plant Sci* **7**:1–12.  
1318 doi:10.3389/fpls.2016.00167
- 1319 Tomizioli M, Lazar C, Brugière S, Burger T, Salvi D, Gatto L, Moyet L, Breckels LM, Hesse A-  
1320 M, Lilley KS, Seigneurin-Berny D, Finazzi G, Rolland N, Ferro M. 2014. Deciphering  
1321 Thylakoid Sub-compartments using a Mass Spectrometry-based Approach. *Mol Cell*  
1322 *Proteomics* **13**:2147–2167. doi:10.1074/mcp.M114.040923
- 1323 Türker C, Akal F, Joho D, Panse C, Barkow-Oesterreicher S, Rehrauer H, Schlapbach R.  
1324 2010. B-Fabric: The Swiss Army Knife for Life Sciences Proceedings of the 13th  
1325 International Conference on Extending Database Technology, EDBT '10. New York, NY,  
1326 USA: Association for Computing Machinery. pp. 717–720. doi:10.1145/1739041.1739135
- 1327 Van Bezouwen LS, Caffarri S, Kale R, Kouřil R, Thunnissen AMWH, Oostergetel GT, Boekema  
1328 EJ. 2017. Subunit and chlorophyll organization of the plant photosystem II supercomplex.  
1329 *Nat Plants* **3**:1–11. doi:10.1038/nplants.2017.80



- 1330 Van Wijk KJ, Kessler F. 2017. Plastoglobuli: Plastid Microcompartments with Integrated  
1331 Functions in Metabolism, Plastid Developmental Transitions, and Environmental  
1332 Adaptation. *Annu Rev Plant Biol* **68**:253–289. doi:10.1146/annurev-arplant-043015-  
1333 111737
- 1334 Von Wettstein D, Gough S, Kannangara CG. 1995. Chlorophyll Biosynthesis. *Plant Cell*  
1335 **7**:1039–1057. doi:10.1105/tpc.7.7.1039
- 1336 Wang BC, Pan YH, Meng DZ, Zhu YX. 2006. Identification and quantitative analysis of  
1337 significantly accumulated proteins during the Arabidopsis seedling de-etiolation process.  
1338 *J Integr Plant Biol* **48**:104–113. doi:10.1111/j.1744-7909.2006.00215.x
- 1339 Weier TE, Brown DL. 1970. Formation of the Prolamellar Body in 8-Day, Dark-Grown  
1340 Seedlings. *Am J Bot* **57**:267–275. doi:10.2307/2485302
- 1341 Wietrzynski W, Schaffer M, Tegunov D, Albert S, Kanazawa A, Plitzko JM, Baumeister W,  
1342 Engel BD. 2020. Charting the native architecture of chlamydomonas thylakoid  
1343 membranes with single-molecule precision. *Elife* **9**:1–18. doi:10.7554/eLife.53740
- 1344 Yoshida Y. 2018. Insights into the mechanisms of chloroplast division. *Int J Mol Sci* **19**:1–13.  
1345 doi:10.3390/ijms19030733
- 1346
- 1347

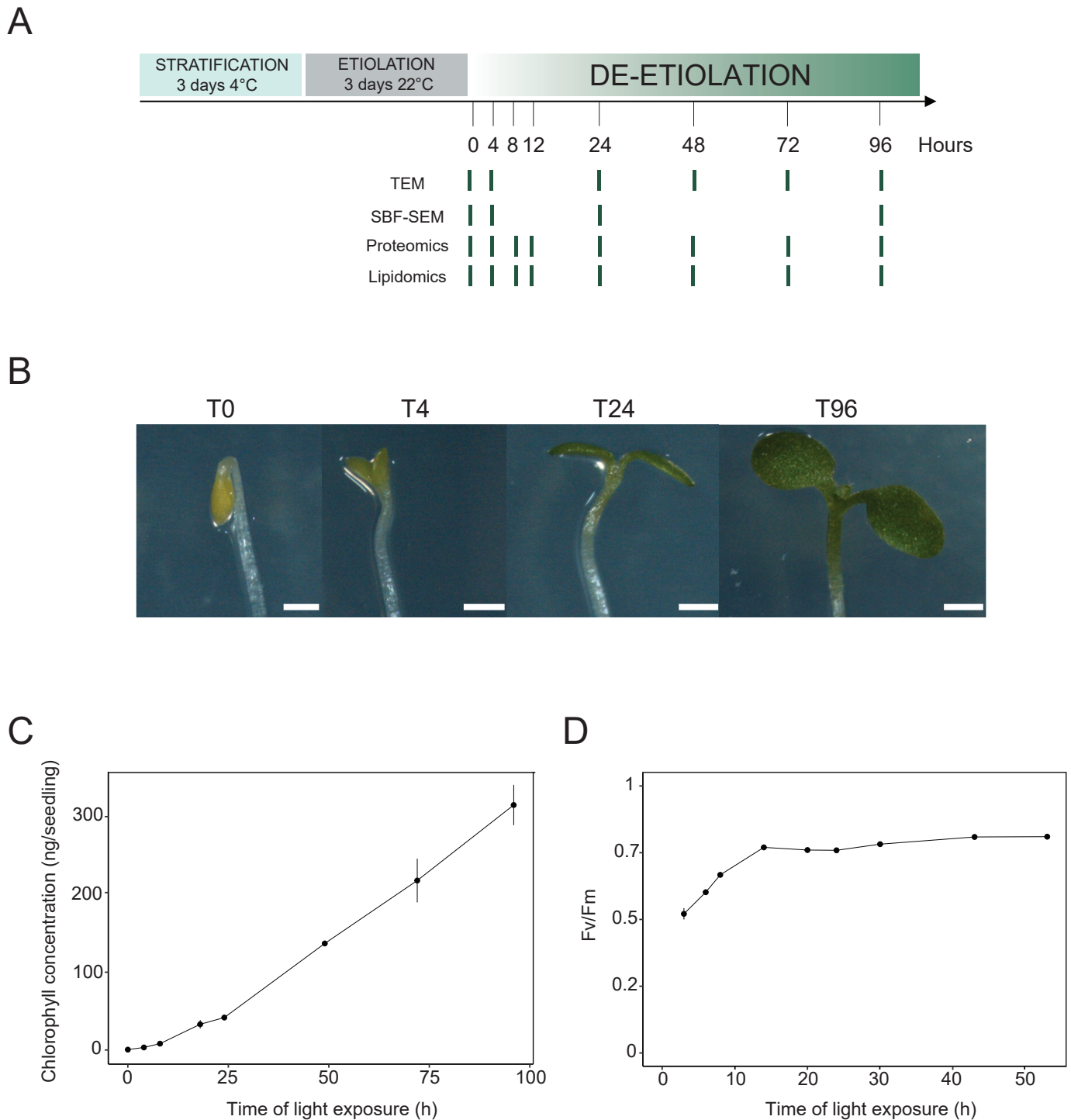


**Figure 1: Photosynthesis onset during de-etiolation. (A) Scheme of the experimental design.** Seeds of *Arabidopsis thaliana* (Columbia) sown on agar plates were stratified for three days at 4°C and then transferred to 22°C in the dark. After three days, etiolated seedlings were exposed to continuous white light (40  $\mu\text{mol}/\text{m}^2/\text{s}$ ) and harvested at different time points during de-etiolation. Selected time points used for different analyses are indicated. (B) Cotyledon phenotype of etiolated seedlings (T0) after 4 h (T4), 24 h (T24), and 96 (T96) h in continuous white light. Scale bars: 0.5 mm. (C) Chlorophyll quantification at different time points upon illumination. Error bars indicate  $\pm$  SD ( $n=3$ ). (D) Maximum quantum yield of photosystem II (Fv/Fm). Error bars indicate  $\pm$  SD ( $n=4-10$ ). For some data points, the error bars are inferior to the size of the symbol. Measurements of further photosynthetic parameters are presented in Figure 1- figure supplement 1.

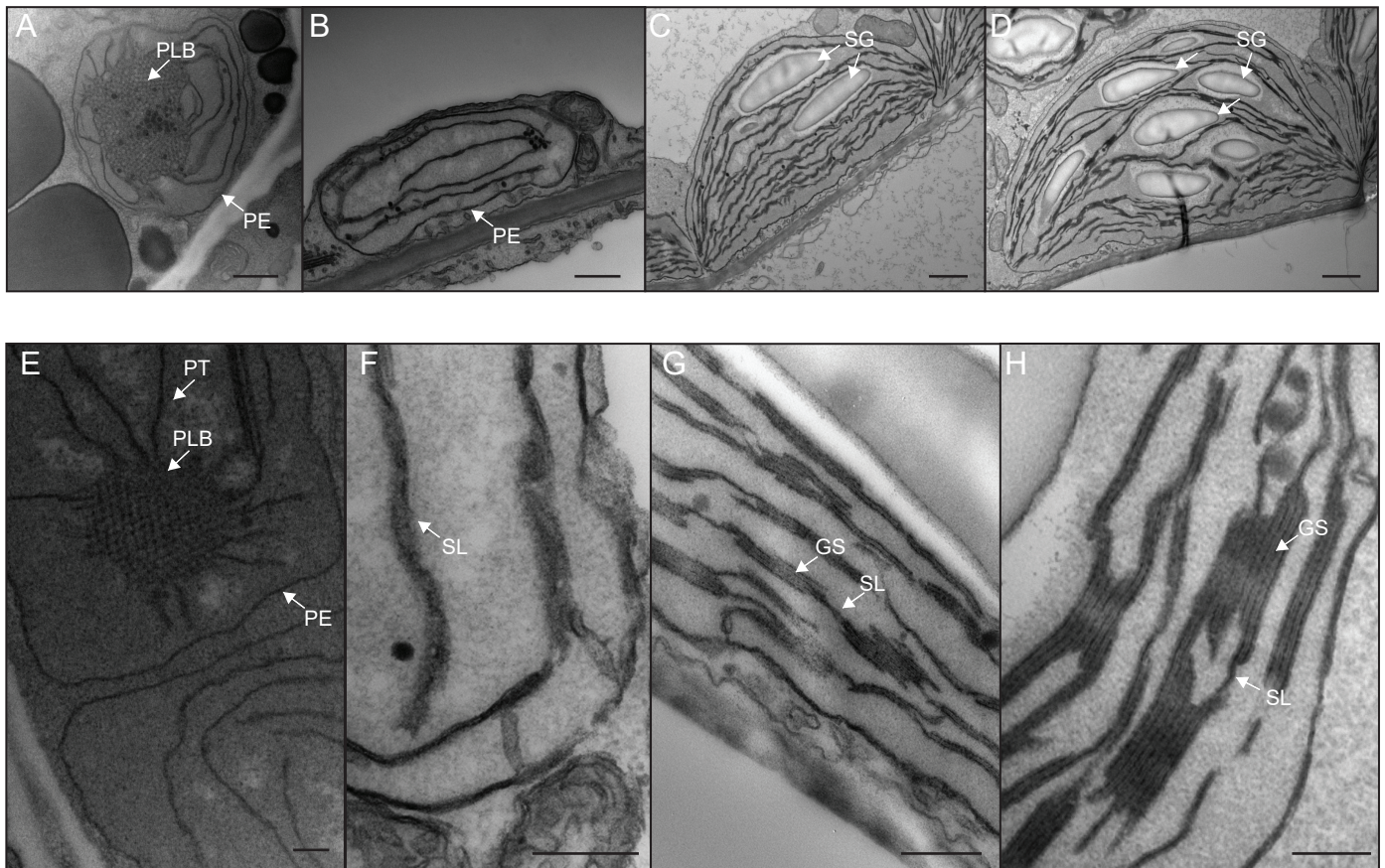


**Figure 2: Qualitative analysis of chloroplast ultrastructure during de-etiolation.** Transmission electron microscopy (TEM) images of cotyledon cells of 3-day-old, dark-grown *Arabidopsis thaliana* (Columbia) seedlings illuminated for 0 h (A and E), 4 h (B and F), 24 h (C and G), and 96 h (D and H) in continuous white light ( $40 \mu\text{mol}/\text{m}^2/\text{s}$ ). (A–D) Scale bars: 500 nm, (E–H) higher magnification of A–D images; Scale bars: 200 nm. PLB: prolamellar body; PT: prothylakoid; PE: plastid envelope; SG: starch grain; GS: grana stack; SL: single lamella. Specific details for measurements of lamella thickness are provided in Figure 2- figure supplement 1.

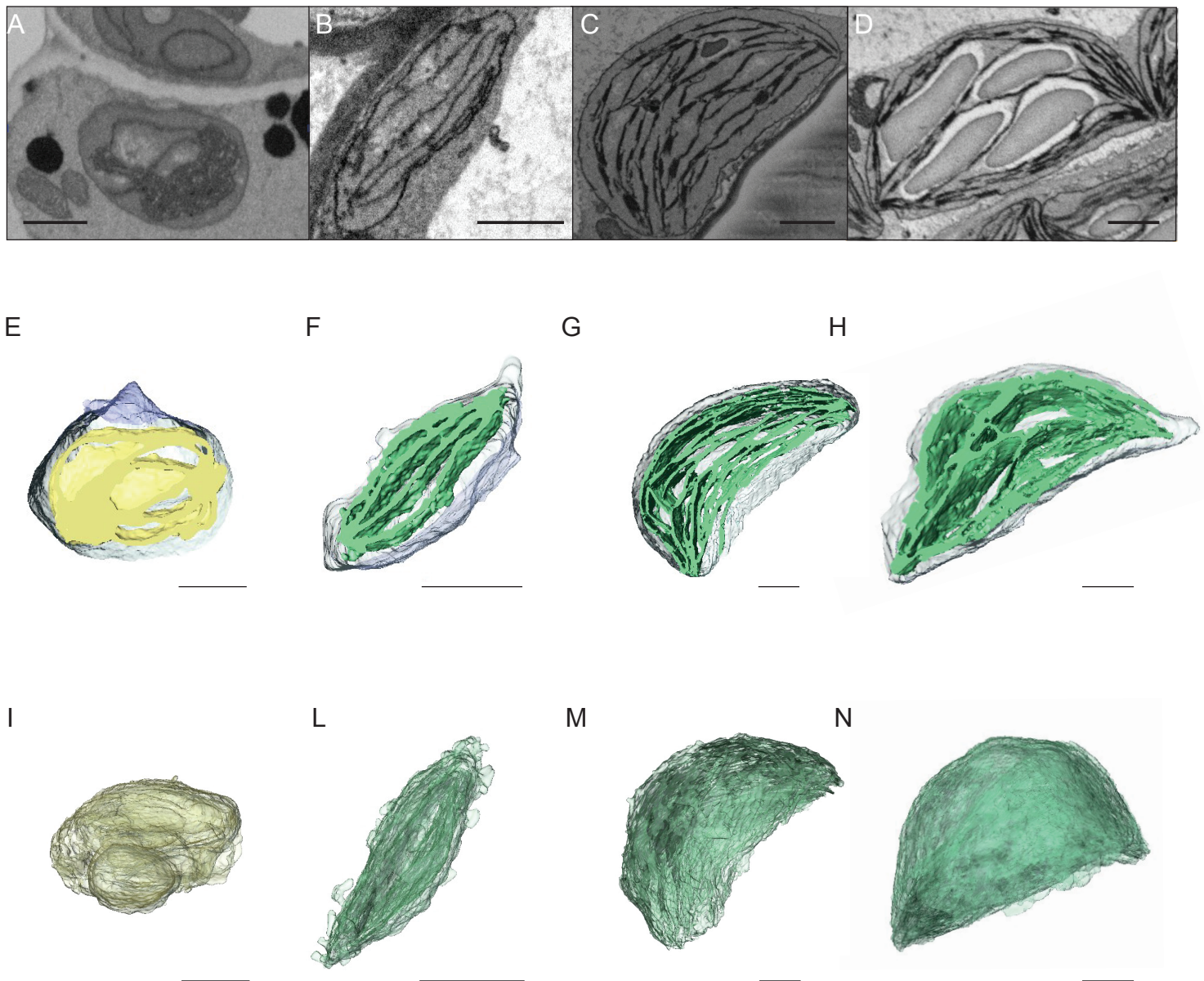
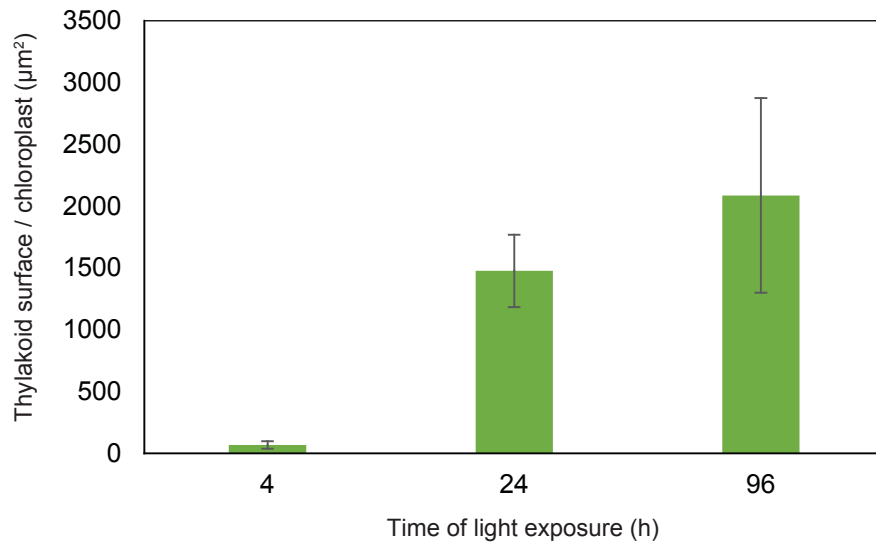


**Figure 3: 3D reconstructions of chloroplast thylakoid network during de-etiolation.** (A–D) Scanning electron microscopy (SEM) micrographs of representative etioplasts and chloroplasts from 3-day-old, dark-grown *Arabidopsis thaliana* seedlings illuminated for 0 h (T0; A), 4 h (T4; B), 24 h (T24; C), and 96 h (T96; D) in continuous white light ( $40 \mu\text{mol}/\text{m}^2/\text{s}$ ). (E–H) Partial 3D reconstruction of thylakoid membranes (green) and envelope (blue) at T0 (E), T4 (F), T24 (G) and T96 (H). Z-depth of thylakoid membrane reconstruction corresponds to  $0.06 \mu\text{m}$  (E),  $0.10 \mu\text{m}$  (F),  $0.13 \mu\text{m}$  (G), and  $0.15 \mu\text{m}$  (H). (I–N). 3D reconstruction of a thylakoid membrane of an etioplast at T0 (I) or a chloroplast at T4 (L), T24 (M), and T96 (N). Scale bars =  $1 \mu\text{m}$ . Details of grana segmentation at T24 are provided in Figure 3- figure supplement 1.

A



B

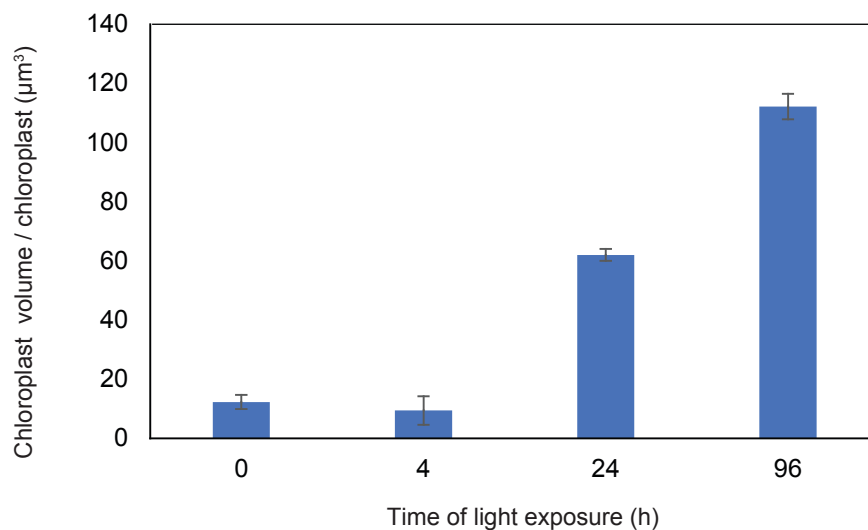


**Figure 4: Quantitative analysis of chloroplast volume and thylakoid surface during de-etiolation.** Quantification of thylakoid surface per chloroplast (A) and chloroplast volume (B) using 3-day-old, dark-grown *Arabidopsis thaliana* (Columbia) seedlings illuminated for 0 h, 4 h, 24 h, and 96 h in continuous white light ( $40 \mu\text{mol}/\text{m}^2/\text{s}$ ). Morphometric data were quantified by Labels analysis module of Amira software. Error bars indicate  $\pm$  SD ( $n=3$ ). The total thylakoid surface indicated in A corresponds to the thylakoid surface exposed to the stroma, calculated in Amira software, in addition to the percentage of the grana surface (%Gs) calculated as described in Figure 3- figure supplement 1.

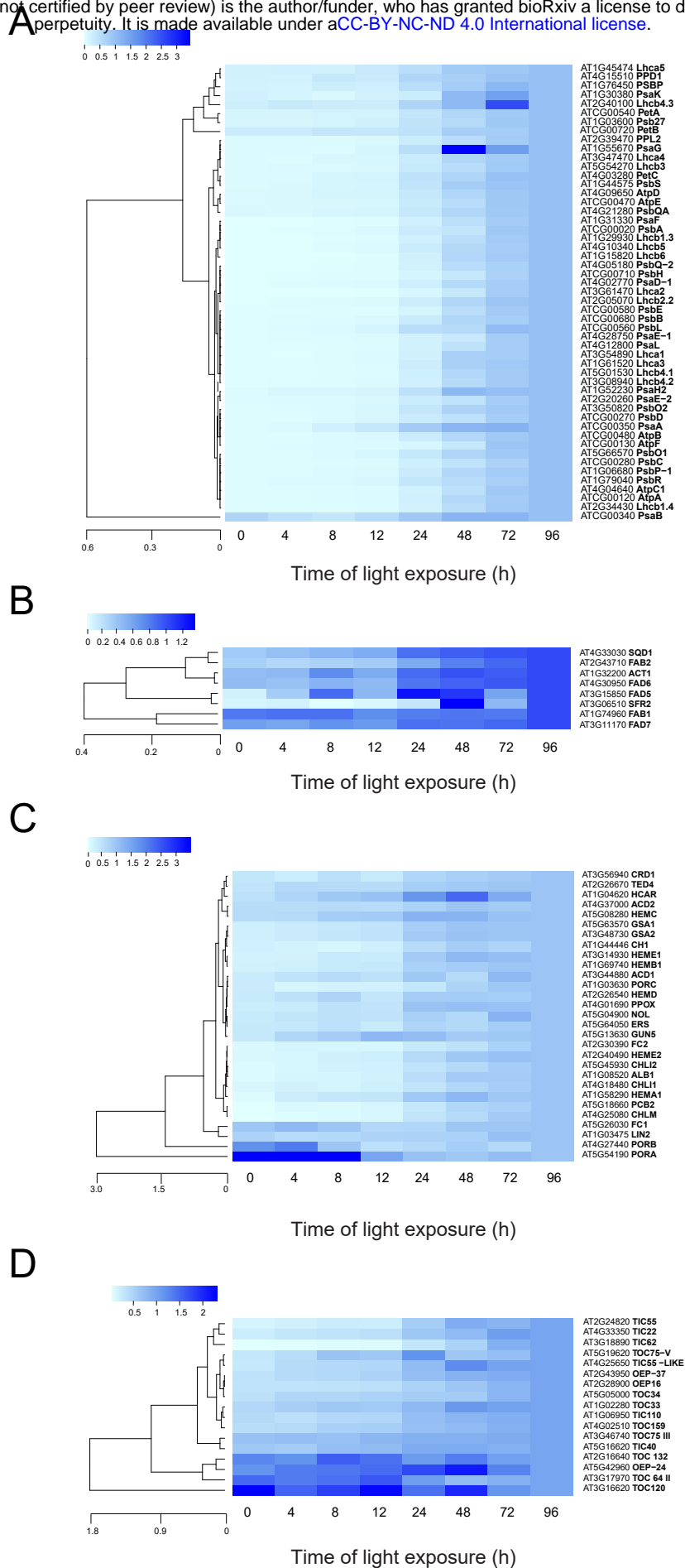
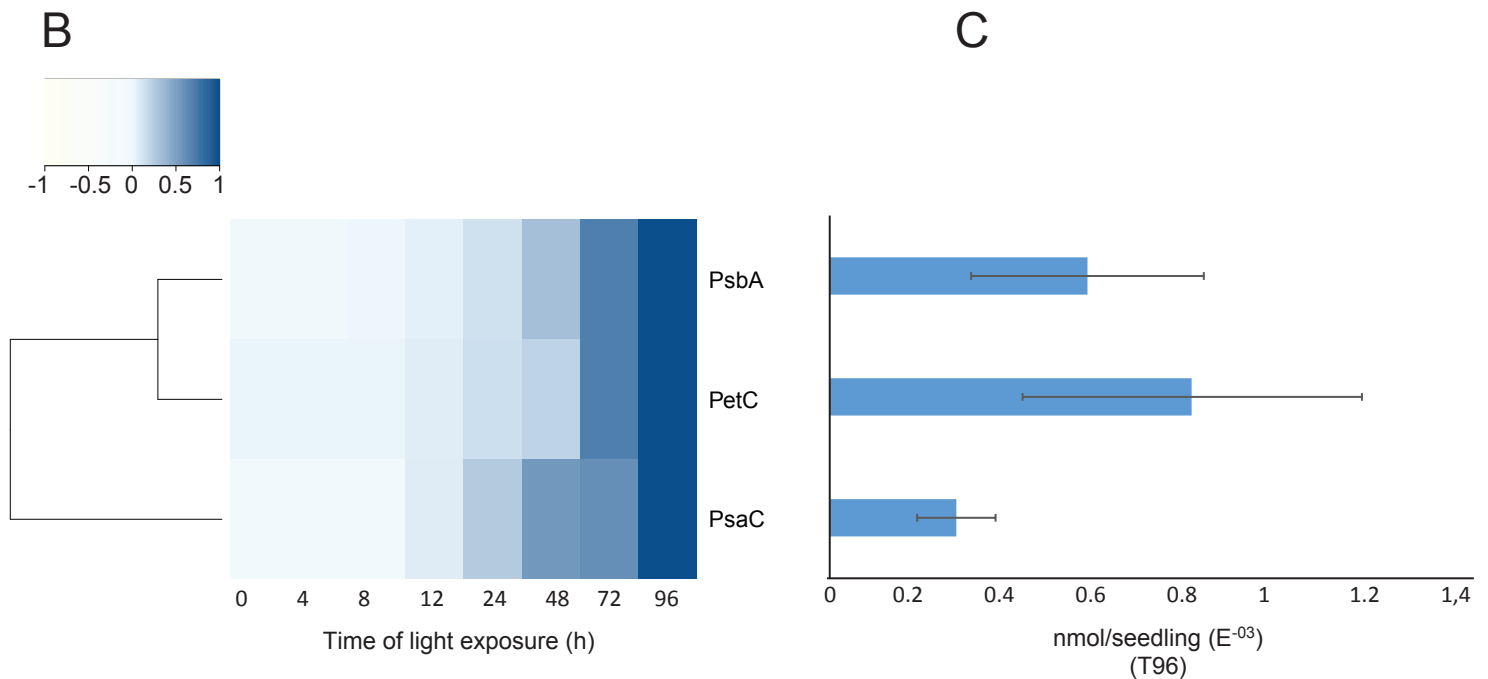
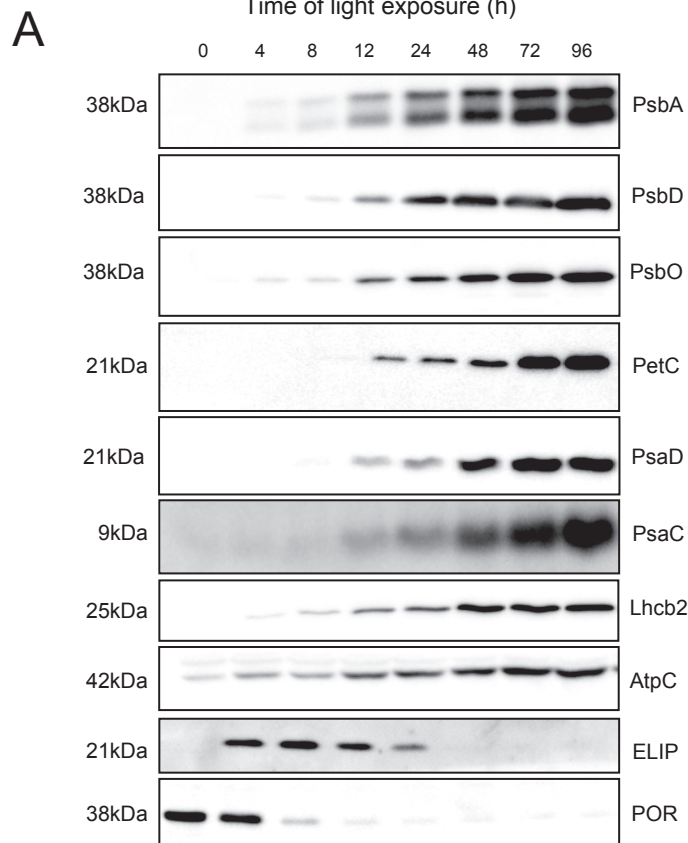
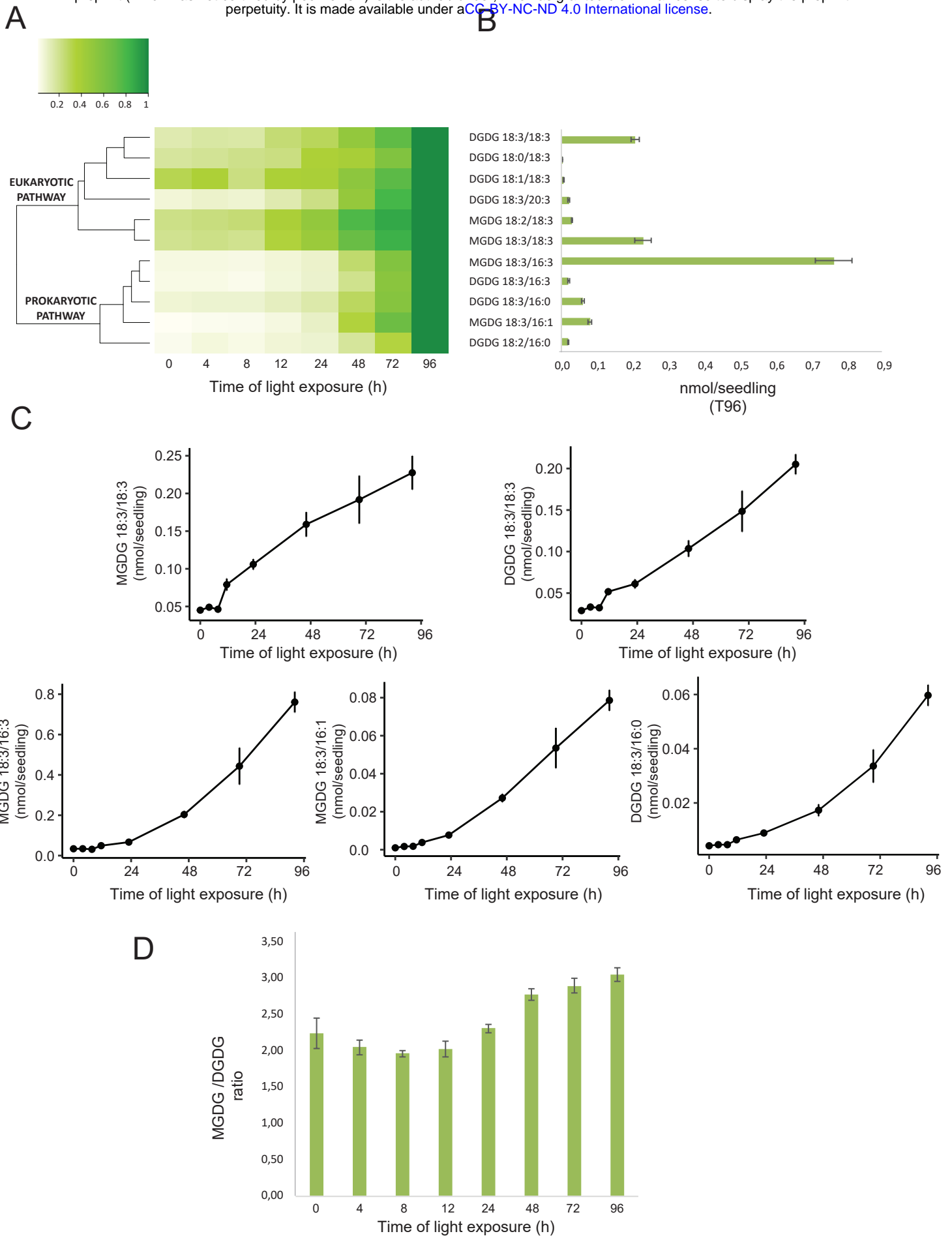


Figure 4: Quantitative analysis of chloroplast volume and thylakoid surface during de-etiolation. Quantification of thylakoid surface per chloroplast (A) and chloroplast volume (B) using 3-day-old, dark-grown *Arabidopsis thaliana* (Columbia) seedlings illuminated for 0 h, 4 h, 24 h, and 96 h in continuous white light (40  $\mu\text{mol}/\text{m}^2/\text{s}$ ). Morphometric data were quantified by Labels analysis module of Amira software. Error bars indicate  $\pm$  SD ( $n=3$ ). The total thylakoid surface indicated in A corresponds to the thylakoid surface exposed to the stroma, calculated in Amira software, in addition to the percentage of the grana surface (%Gs) calculated as described in Figure 3- figure supplement 1.



**Figure 6: Accumulation dynamics of photosynthesis-related proteins during de-etiolation.** 3-day-old etiolated seedlings of *Arabidopsis thaliana* were illuminated for 0 h (T0), 4 h (T4), 8 h (T8), 12 h (T12), 24 h (T24), 48 h (T48), 72 h (T72), and 96 h (T96) under white light ( $40 \mu\text{mol}/\text{m}^2/\text{s}$ ). (A) Proteins were separated by SDS-PAGE and transferred onto nitrocellulose membrane and immunodetected with antibodies against PsbA, PsbD, PsbO, PetC, PsaD, PsaC, Lhcb2, AtpC, ELIP, POR proteins. (B–C) Quantification of PsbA, PetC, and PsaC during de-etiolation. Heatmap (B) was generated after normalization of the amount of each protein relative to the last time point (T96). Graph (C) corresponds to the absolute quantification of proteins at T96. Error bars indicate  $\pm$  SD ( $n=3$ ). Quantification of photosystem-related proteins during de-etiolation is detailed in Figure 6- figure supplement 1.



**Figure 7: Accumulation dynamics of galactolipids during de-etiolation.** 3-day-old etiolated seedlings of *Arabidopsis thaliana* were illuminated for 0 h (T0), 4 h (T4), 8 h (T8), 12 h (T12), 24 h (T24), 48 h (T48), 72 h (T72), and 96 h (T96) under white light (40  $\mu\text{mol}/\text{m}^2/\text{s}$ ). (A) Heatmap representation of galactolipids (MGDG and DGDG) during de-etiolation. Samples were normalized to the last time point (T96). (B) Absolute quantification at T96 expressed in nmol/seedling. Error bars indicate  $\pm$  SD (n=4). (C) Absolute quantification (nmol/seedling) of the most abundant chloroplast galactolipids MGDG (MGDG 18:3/18:3, MGDG 18:3/16:3, MGDG 18:3/16:1) and DGDG (DGDG 18:3/18:3, DGDG 18:3/16:0) at different time points during de-etiolation. Error bars indicate  $\pm$  SD (n=4). (D) The MGDG/DGDG ratio was calculated using all 12 species of galactolipids detected during de-etiolation. Error bars indicate  $\pm$  SD (n=4).



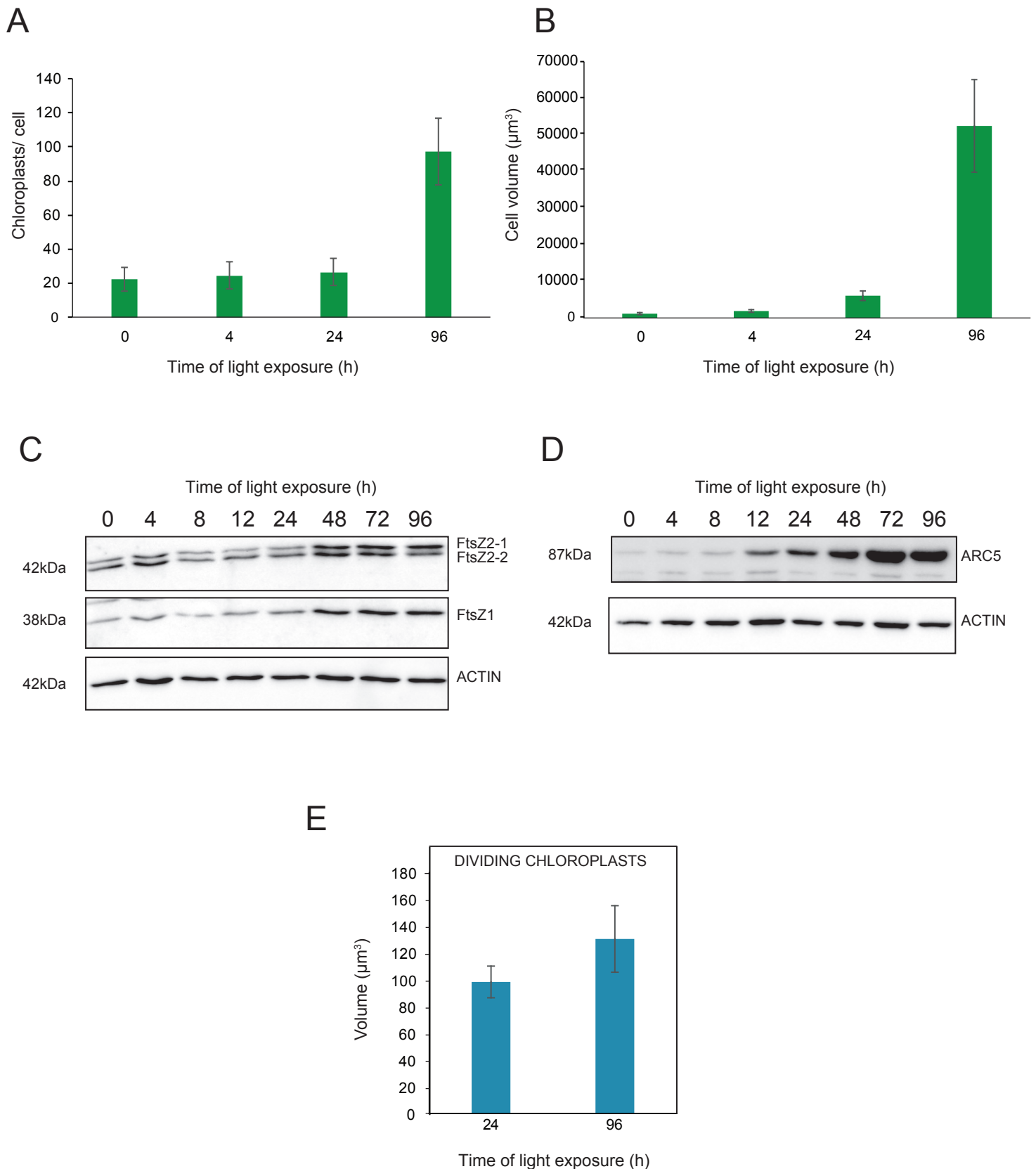


**Figure 8: Relationship between chloroplast proliferation and chloroplast volume.** (A-B) Chloroplast number and cell volume in cotyledons of 3-day-old, dark-grown *Arabidopsis thaliana* seedlings illuminated for 0 h (T0), 4 h (T4), 24 h (T24), and 96 h (T96) in continuous white light ( $40 \mu\text{mol}/\text{m}^2/\text{s}$ ). (A) Chloroplast number per cell during de-etiolation. Error bars indicate  $\pm$  SD ( $n=6$  for T0 and T7; 7 for T24; 5 for T96). (B) Cell volume was quantified by the Labels analysis module of Amira software. Error bars indicate  $\pm$  SD ( $n=5-6$ ). (C-D) Total proteins were extracted from T0-T96 seedlings, separated on SDS-PAGE, and transferred onto nitrocellulose. Proteins involved in plastid division (C, FtsZ; D, ARC5) and loading control (actin) were detected using specific antibodies (FtsZ2 antibody recognizes both FtsZ2-1 and FtsZ2-2). (E) Volume of dividing chloroplast at T24 and T96. Error bars indicate  $\pm$  SD ( $n=3$ ). Further details of chloroplast proliferation in parallel with cell expansion are provided in Figure 8- figure supplement 1.

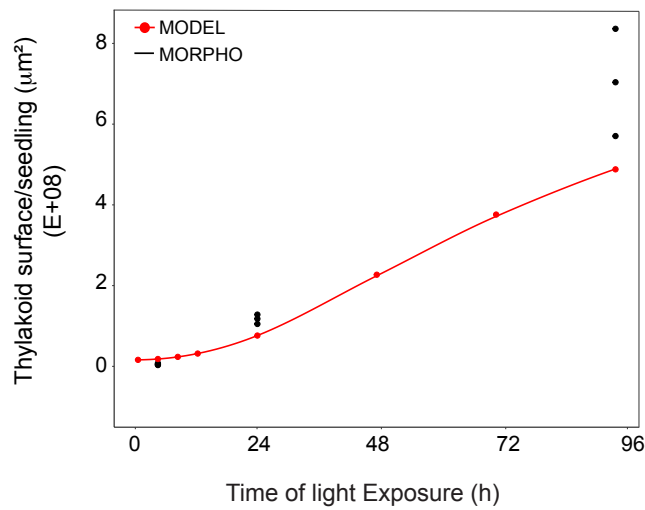


**Figure 9: Superimposition of thylakoid surface per seedling obtained from morphometric analysis and mathematical modeling.** Thylakoid surface per seedling was estimated using quantitative data from 3View analysis ('MORPHO' black dots at T4, T24, and T96; and see Figure 4 and Table 1) and model generated using the quantitative data from proteomics and lipidomics ('MODEL' red line at T0, T4, T8, T12, T24, T48, T72, and T96, and Table 1). Further details are provided in Figure 9- figure supplement 1 and 2.

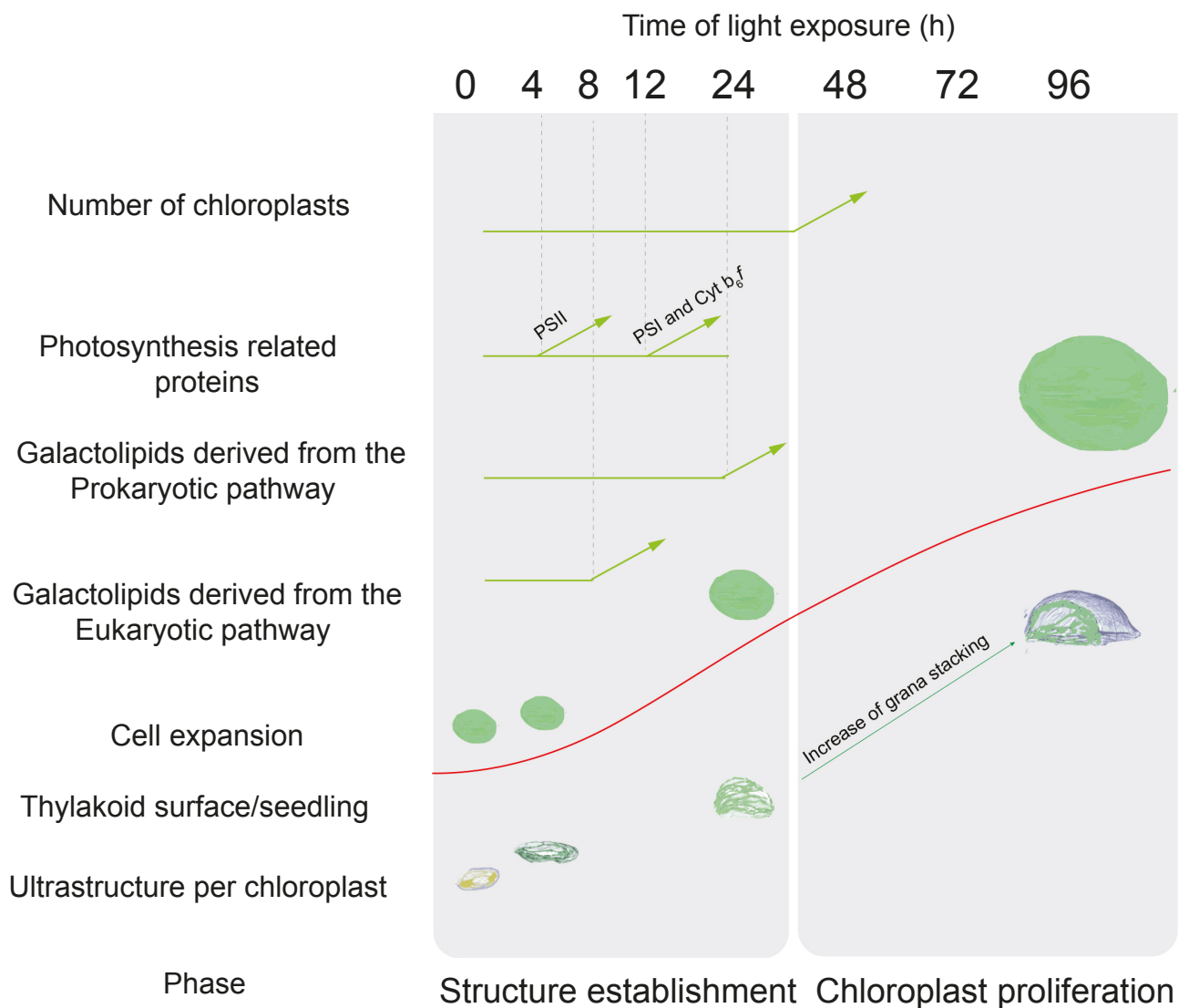


**Figure 10: Overview of changes observed during the de-etiolation process in *Arabidopsis thaliana* seedlings.** The ‘Structure Establishment Phase’ is correlated with disassembly of the PLB and gradual formation of the thylakoid membrane as well as an initial increase of eukaryotic (after 8 h) and prokaryotic (after 24 h) galactolipids and photosynthesis-related proteins (PSII subunits at 4 h, PSI and cyt b<sub>6</sub>f at 12 h). The subsequent ‘Chloroplast Proliferation Phase’ is associated with an increase in chloroplast number in concomitance with cell expansion, a linear increase of prokaryotic and eukaryotic galactolipids and photosynthesis-related proteins, and increased grana stacking. The red curve (retrieved from the Figure 9) shows thylakoid surface/seedling dynamics during the de-etiolation process.